Department of Precision and Microsystems Engineering

Enhancing FRET Signal Accuracy in DNA Origami Structures Using Gold Nanoarrays

Arland Sidoel

Report no : 2025.056
Coach : Ze Yu, Daria Orekhova
Professor : Sabina Caneva
Specialisation : DMN
Type of report : Thesis
Date : 15-08-2025

Abstract

The bottom-up manufacturing of DNA origami structures allows for precise control of DNA-based nanostructures' shape, size, and functionality, making it a powerful tool in nanotechnology. Single-molecule fluorescence measurements, including Forster resonance energy transfer (FRET), are often used to visualise the nanoscale movements of these structures. However, FRET is prone to crosstalk when labelled structures are within a 10 nm range of each other. DNA origami immobilisation within nanoarrays can minimise the crosstalk, since their spatial spacing would be beyond the effective FRET range.

This research aimed to generate nanoarrays with at least 5x5 binding spots and develop a method for filling up this nanoarray with at least 50% DNA origami structures without altering their dynamics. Using nanosphere lithography (NSL), a technique in which the nanospheres self-assemble into a hexagonal closed-packed (HCP) structured monolayer mask, with 300, 600, and 800 nm nanospheres, two types of nanoarrays were fabricated. (1) Oxygen plasma exposure of the nanosphere of the mask, followed by gold sputtering, resulted in binding spots with a diameter as small as 191.1 nm for biotin-BSA surface functionalization. (2) Heat treatment of the nanosphere mask, reducing the hole size between nanospheres to a minimum of 60 nm. Annealing resulted in regularly spaced small gold islands with a diameter of ∼173.2 nm for thiol-modified DNA immobilization. Both array types were able to create 5x5 binding spot areas confidently.

Fluorescent experiments were performed to analyse the nanoarray occupancy and Holliday Junctions (HJ) dynamics. Within the reduced sphere size via oxygen plasma treatment array, ∼4.3% of 700 analysed traces were HJs, while only ∼0.7% showed their characteristic switching states. Therefore, the proposed method did not reach the occupancy goal of 50%, but the HJ dynamics were preserved. Two traces within the array were compared with baseline traces and gave t-values of 0.59 and 8.73, indicating no significant change in dynamics.

The novelty of using gold sputtering to create nanoarrays while placing a dynamic DNA origami structure (HJ) led to functional DNA behaviour, as verified by their dynamics, but more research is required to optimise further the results found.

Table of Contents

1 Introduction

DNA origami nanotechnology is a technique that allows for the precise control of shape, size, and functionality of nanostructures built entirely out of nucleic acids [1]. This makes DNA origami a powerful tool in nanotechnology. DNA origami nanostructures have drawn interest in biotechnology due to their diverse applications. They can act as precise molecular channels for controlled transport of analytes [2], they can be used in biosensing applications to detect specific molecules [3], [4], and serve as drug delivery systems enabling targeted and controlled release of therapeutic agents [5], [6].

However, due to the small size of typical DNA origami structures (<100 nm), studying their dynamic behaviour often requires fluorophores. Fluorophores are light-emitting molecules that can be excited by specific wavelengths. These molecules can then be strategically placed on the DNA origami structures to enable a process known as Förster resonance energy transfer (FRET), which allows an analysis to study the dynamics of the DNA origami structure. A distant dependent FRET signal comes from a FRET donor and acceptor pair attached to a nanostructure under investigation [7], [8]. FRET provides real-time information about structural changes within the DNA nanostructures by revealing the variation in the fluorescence properties of the fluorophores.

During a conventional white light or fluorescence experiment, a signal is detected from a bulk (ensemble) sample containing 10^5 or more molecules [9]. These combined signals do not indicate the individual emissions molecules. Instead, it provides an averaged signal from all molecules in the field of view. A schematic overview of both signals is shown in Figure 1. In Figure 1a, the emission of multiple single molecules is shown to add up as a single peak emission. The individual contribution of each molecule is not visible in the measured result. A similar situation is illustrated in Figure 1b, where the average of three FRET signals looks like a constant signal while the individual signals have peaks and valleys.

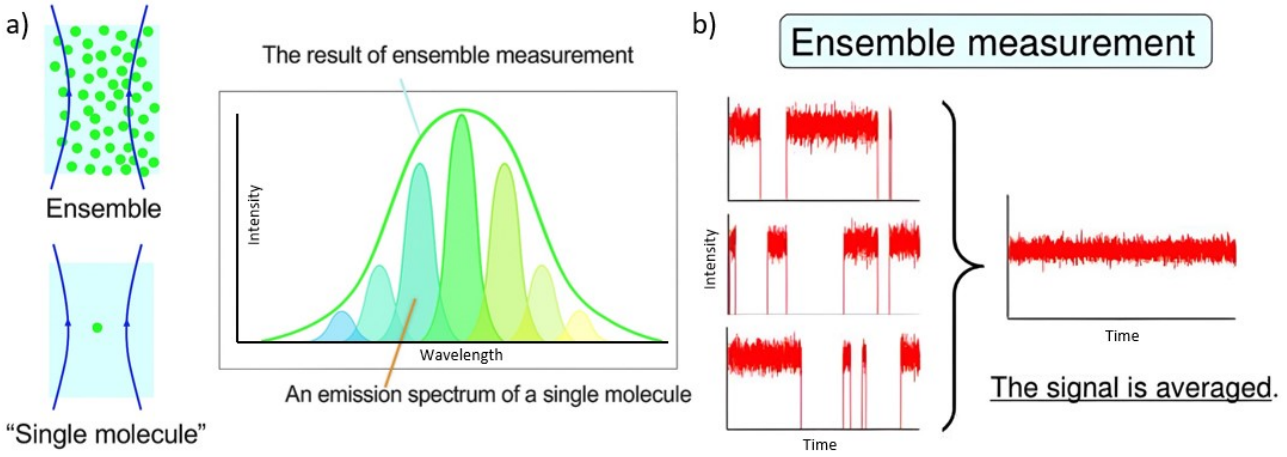

Figure 1: (a) Combined emission from ensemble measurement (b) Averaged FRET signal formed by three individual signals [10].

Given the stochastic nature of single-molecule dynamics, it is essential to reveal the behaviour of individual molecules. Hidden sub-populations or non-abundant molecules also risk being averaged out from ensemble data. During single-molecule measurements, the molecules need to be isolated from other molecules. This will prevent crosstalk between samples, preventing a more ambiguous signal, where the state of one nanostructure can interfere with the response of an adjacent structure. Furthermore, a single molecule's signal is weaker than that of multiple molecules in a diffraction-limited area. These combined stronger signals make data analysis more challenging since the weaker signals from a single molecule might look like noise. These limitations can limit FRET measurement's reliability and data throughput, given that it is a highly distance-dependent phenomenon.

By using nanoarrays for FRET, these limitations can partly be overcome. These arrays will have defined patterns of binding spots for DNA origami structures. By controlling the concentration of DNA origami structures, the precise and ordered placement of individual structures will be enabled, preventing many molecules from being on a single spot and limiting crosstalk effects in the measurements. Despite the potential of using nanoarrays for FRET, few studies combine precise positioning of nanostructures and instead rely on the random distribution of structures on a surface. In current literature, expensive specialized equipment or toxic chemicals are used

to fabricate the nanoarray [11]–[13]. This makes the fabrication complex and harms the environment and the researcher. Therefore, there is a need for a simple method using non-toxic chemicals.

This research will develop a methodology to generate gold nanoarrays using non-toxic chemicals to reduce crosstalk in fluorescence measurements, how DNA origami structures can be placed in such nanoarrays, and how the dynamics of DNA origami structures are affected when placed in nanoarrays. To answer these questions, two potential methods for achieving usable nanoarrays for FRET are explored. Additionally, fluorescent characterisation techniques will be used to analyse the performance of the two nanoarrays in single-molecule measurements.

The two methods for the fabrication of nanoarrays are based on nanosphere lithography (NSL), which utilizes the physical properties of the nanospheres to generate arrays and 'inverted' arrays. Here, the DNA origami nanostructures are placed in the gaps left by the spheres or between the spheres (inverted array). The first method will use oxygen plasma exposure to etch the nanospheres, which decreases their size. The non-exposed region under the spheres will decrease, creating a small binding spot for a DNA origami structure. For inverted arrays, the second method uses the glass transition temperature (T_g) of the nanospheres to partly melt the nanospheres and fuse them together at their contact points. As a result, small gaps will remain in the mask. Small regularly spaced dots remain after (gold) deposition and mask removal. DNA origami structures can be chemically modified to bind to these dots. A schematic overview of both methods is shown in Figure 2. To verify both methods, an FRET analysis was performed using a simple FRET ruler and a Holliday Junction, since their behaviour is well-studied.

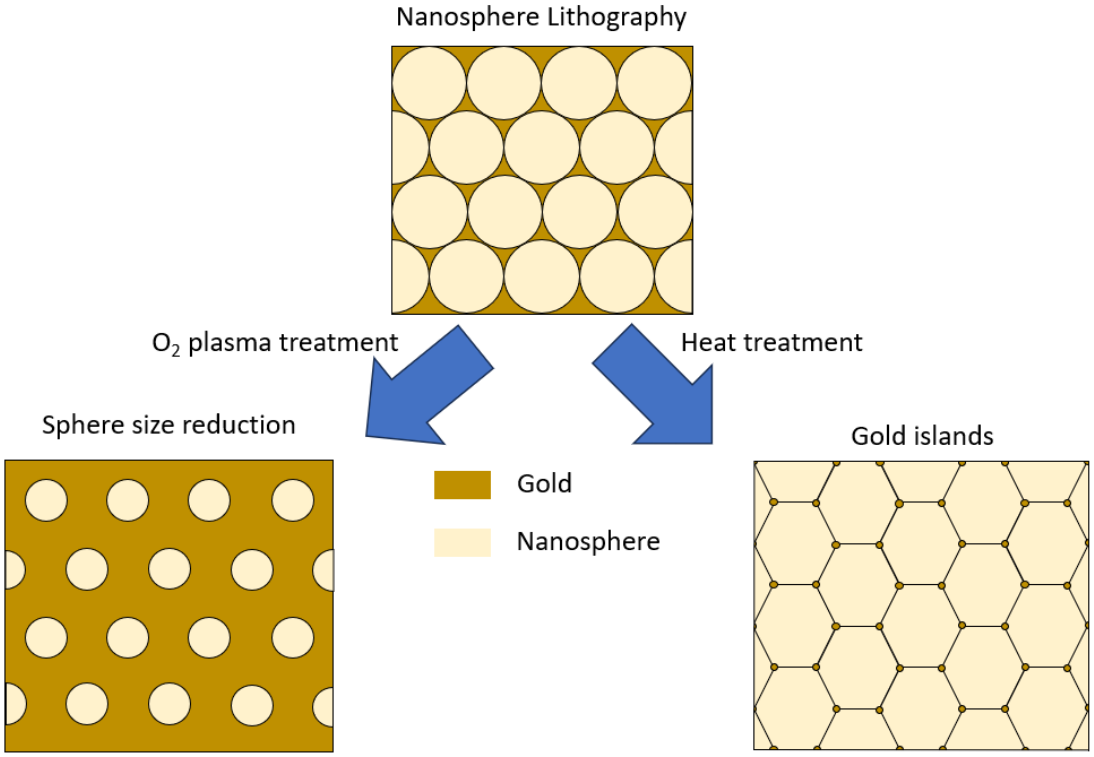

Figure 2: Methods to achieve individual binding spots for DNA origami structures.

While configurable DNA nanostructures have great potential in biotechnology, their characterization requires improved methods to study their dynamics and mechanics at the structural level. However, the use of nanoarrays to improve FRET for DNA origami actuators has not yet been explored. Therefore, this thesis aims to improve the FRET signal accuracy of DNA origami structures. This thesis addresses the fabrication of nanoarrays and the optical characterization of static and dynamic model DNA nanostructures to validate the signal improvement.

2 Background

This section provides an overview of the key concepts and techniques relevant to this project. First, the principle behind DNA origami is explained. Secondly, a comparison is made between fluorescence imaging techniques to capture the dynamics of DNA origami structures. Furthermore, two different immobilizing techniques are mentioned. Lastly, various methods for generating nanoarrays will be introduced, and the chosen technique, nanosphere lithography, will be elaborated in more detail.

2.1 DNA origami

In 1982, Prof. N.C. Seeman first proposed using DNA to create precise nanoscale structures. Since then, DNA technology has been the subject of extensive research [14]. This powerful technique is known for its high yield of identical nanostructures that can be built with single-base resolution. Two potential future applications for DNA nanostructures can be found in drug delivery and nanorobotics. The engineered DNA nanostructure could transport drugs in a box-like structure. The box can then open at the desired location, responding to environmental triggers such as specific molecules, pH, or enzymatic activity. Such a method would minimize the side effects of drugs and improve treatment efficiency. In nanorobotics, DNA structures will be able to perform mechanical tasks. For example, the structure can change its shape dynamically, which can be used to study the force-displacement relation at the nanoscale or exert mechanical forces on other objects [15].

The concept of reshaping DNA into any desired structure lies in the structure and chemical composition of the molecule. DNA has a double helix structure consisting of two complementary single-stranded DNA (ssDNA) strands. Each ssDNA strand has a repeating sugar-phosphate backbone, providing structural stability and a sequence of nitrogenous bases. DNA has four different types of nitrogenous bases: adenine (A), thymine (T), cytosine (C), and guanine (G). With the Watson-Crick base pairing principle, A pairs with T and C with G via hydrogen bonds. This pairing enables the ssDNA strands to hybridize and form a double-stranded DNA (dsDNA) with a helical conformation.

DNA origami is a method to fabricate DNA nanostructures. The name refers to the Japanese art of folding paper, since with DNA origami, long ssDNA scaffolds are folded into the predefined structure through hybridization with shorter ssDNA staple strands [1]. Eventually, complex structures can be produced with the clever selection of staple sequence, length, and placement. Some examples of 2D DNA nanostructures are shown in Figure 3. The self-assembly happens under heated conditions (thermal annealing) in which the DNA mixture is heated to about 90°C and then cooled down to room temperature. This process allows the staple strands to hybridize to the scaffold under ideal conditions and therefore reshape the scaffold into the pre-designed shape [14].

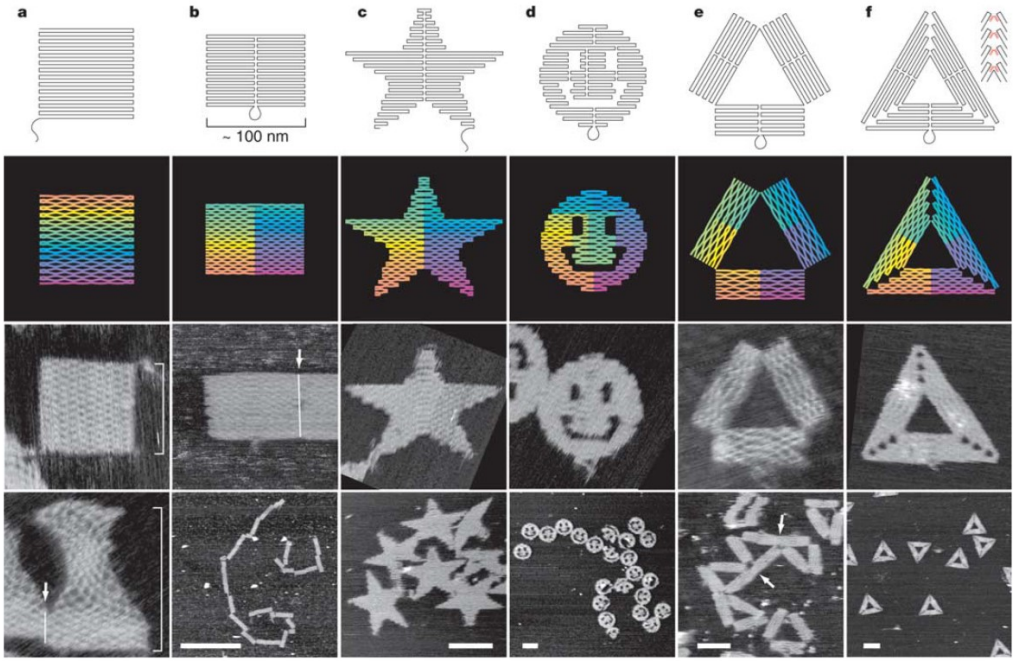

Figure 3: Examples of 2D DNA nanostructures manufactured with DNA origami [1].

These DNA structures are static; however, reconfigurability can be achieved by external stimuli such as strand displacement [16], [17]. Such reconfigurable structures often use flexible single-stranded DNA segments from scaffold parts to act as a 'hinge'. Such designs can thus change states via trigger strands that interact with the flexible single-stranded DNA segments. For example, the trigger strand can hybridize with the segments, increasing its stiffness and thus changing the mechanism's shape and size [16], [17]. This process can then be reversed by introducing anti-trigger strands in the solution. A schematic overview of the process is shown in Figure 4. The overextending segment h*, a toehold, hybridizes with the anti-trigger strand, resulting in flexible single-stranded segments (blue segment).

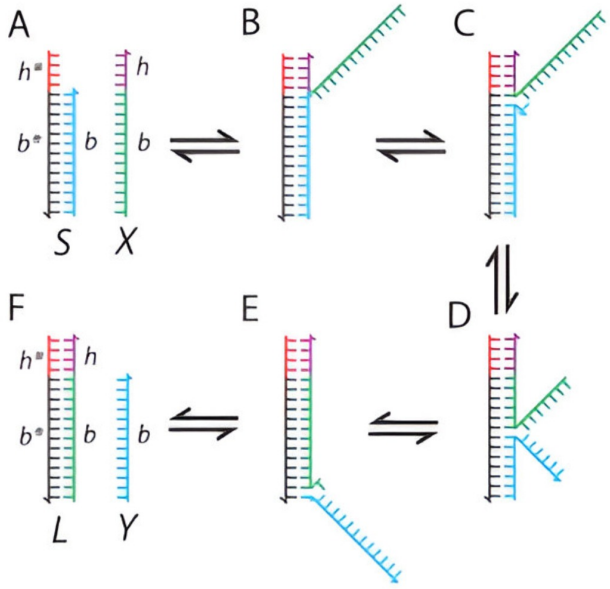

Figure 4: Toehold-mediated strand displacement via three-way branch migration [17].

2.2 Fluorescence imaging techniques

Fluorescence imaging techniques are essential for visualizing and analyzing the dynamic behavior of DNA origami structures with high precision. FRET, STORM, and DNA-PAINT are techniques used for studying nanoscale biological systems. This subsection will explore these techniques in detail, highlighting their strengths and limitations.

Fluorescence imaging techniques are noninvasive techniques that allow real-time study of molecules or complex biological systems. For this phenomenon, fluorophores absorb photons at one wavelength (excitation) and then emit light at a longer wavelength (emission). When a fluorophore absorbs a photon, its electrons are excited to a higher energy level. After a short time, the electrons release energy through heat and a photon as they return to their ground state in nanoseconds. The emitted light has a lower energy and thus a longer wavelength than the absorbed light [7], [8].

2.2.1 FRET

FRET is a fluorescence-based imaging technique that measures the nonradiative energy transfer between a fluorophore donor-acceptor pair. The energy transfer occurs when the donor's emission spectrum partially overlaps with the acceptor's absorption spectrum [7], [8]. The Jablonski diagram of the electron energy states is shown in Figure 5. Compared to regular FRET, the energy is transferred to the acceptor molecule instead of emitting a photon. The efficiency of this phenomenon is highly distance-dependent (1-10 nm). The formula for the FRET efficiency is given in Equation 1 [8]. Where r equals the distance between the fluorophore, r_0 equals the Förster distance where $E_{FRET} = 0.5$, F_A is the acceptor emission, and F_D equals the donor emission. A schematic FRET efficiency diagram is shown in Figure 5.

$$E_{FRET} = \frac{1}{1 + (\frac{r}{r_o})^6} = \frac{F_A}{F_D + F_A} \tag{1}$$

When the donor fluorophore is excited, its energy is transferred to the acceptor fluorophore, causing the acceptor to emit a photon. This unique property makes FRET an excellent tool for studying molecular interactions and molecular dynamics at the nanometer scale.

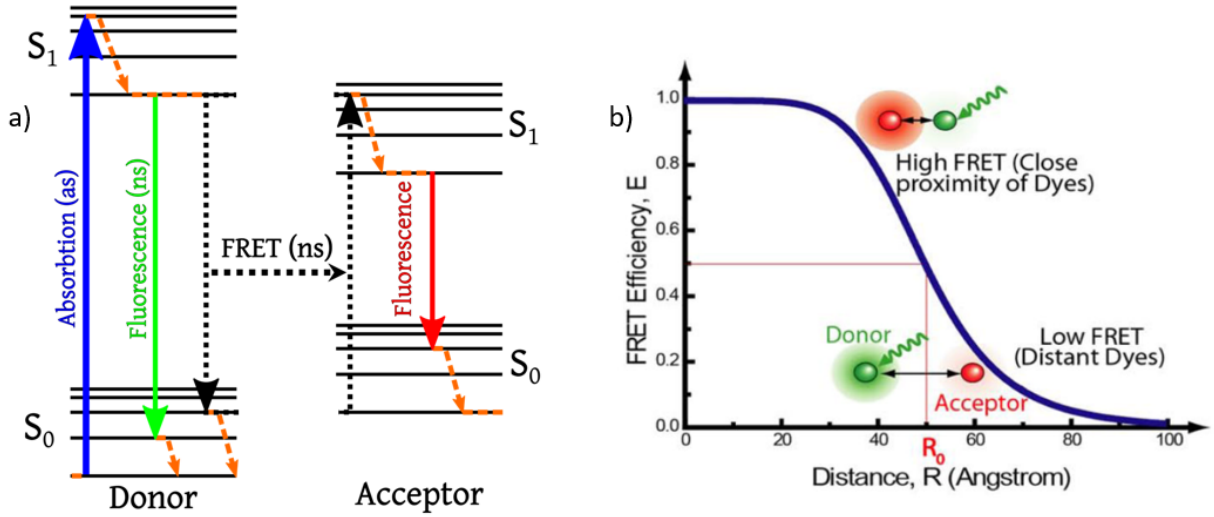

Figure 5: (a) Jablonski diagram of energy states fluorophore [18]. (b) FRET efficiency diagram [7].

Fluorophores, just like staple strands, can be introduced to DNA origami structures. They do not alter the structure's overall shape but can hybridize at a specified location. Adding a FRET pair enables the dynamic behavior study of a DNA origami structure. Two classic examples of DNA origami nanostructures with a FRET pair are FRET rulers and Holliday junctions (HJ). A schematic overview of these structures is shown in Figure 6.

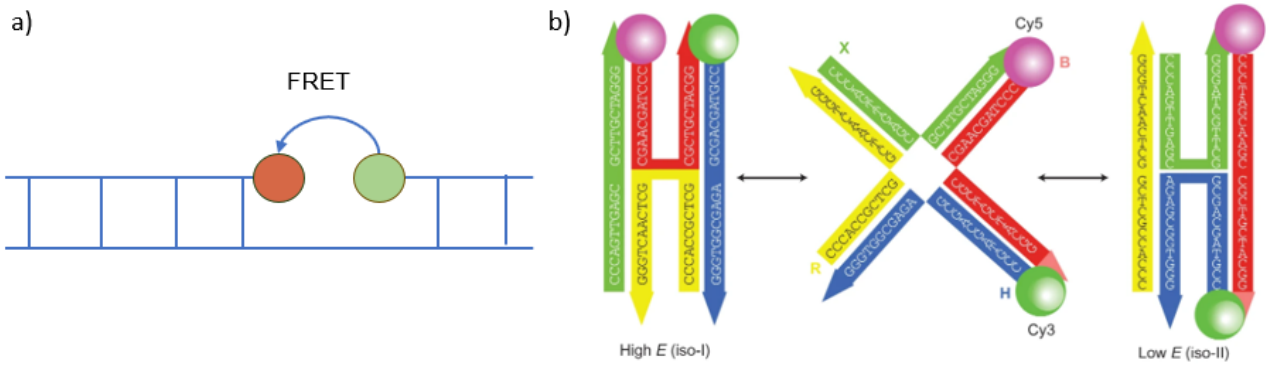

Figure 6: (a) Schematic overview of the structure of a FRET ruler. (b) Schematic overview of the states of an HJ [19].

The FRET traces of these structures show their dynamics. The FRET rulers will have a constant fluorescence signal, while the Holliday junction constantly switches between the closed and open states. An example FRET trace of a Holliday junction is shown in Figure 7. The flipping of the donor and acceptor fluorescence indicates the switching between open and closed state en thus the structure's dynamic behavior.

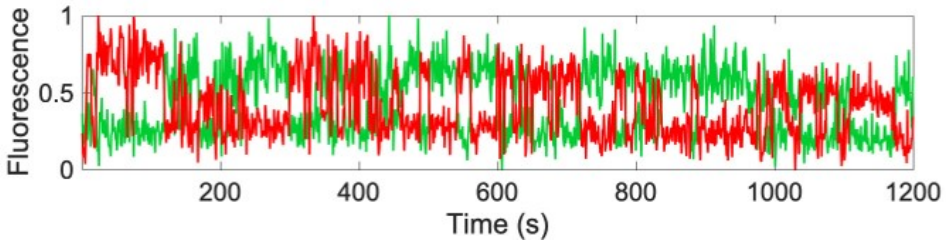

Figure 7: FRET trace of HJ showing switching states [20].

Despite its advantages, FRET has several limitations. One challenge is the requirement for donor-acceptor spectral overlap, which can restrict the choice of fluorophores and complicate experimental design. Additionally, FRET efficiency decreases rapidly with increasing distance, limiting its use to interactions within a very narrow range. Furthermore, quantitative FRET analysis often requires complex calibration and correction for factors such as fluorophore concentration, orientation, and environmental effects. In addition, crosstalk can be a problem. Crosstalk occurs when two pairs are within the 10 nm range of each other. The donor of one pair transfers its energy to the acceptor of the different pair, resulting in a false signal [7], [8].

DNA origami structures analyzed with FRET are often imaged with a total internal reflection fluorescence (TIRF) microscope. Compared with epifluorescence, where the entire sample is illuminated, TIRF only illuminates a small sample layer (60-100 nm) [21]. A schematic overview of the difference in illumination is shown in Figure 8. This difference results in a cleaner signal with less background noise, shown in Figure 8. Furthermore, DNA origami structures need to be immobilized within the illuminated area. The immobilization techniques, suitable for TIRF, will be discussed in more detail in section 2.3.

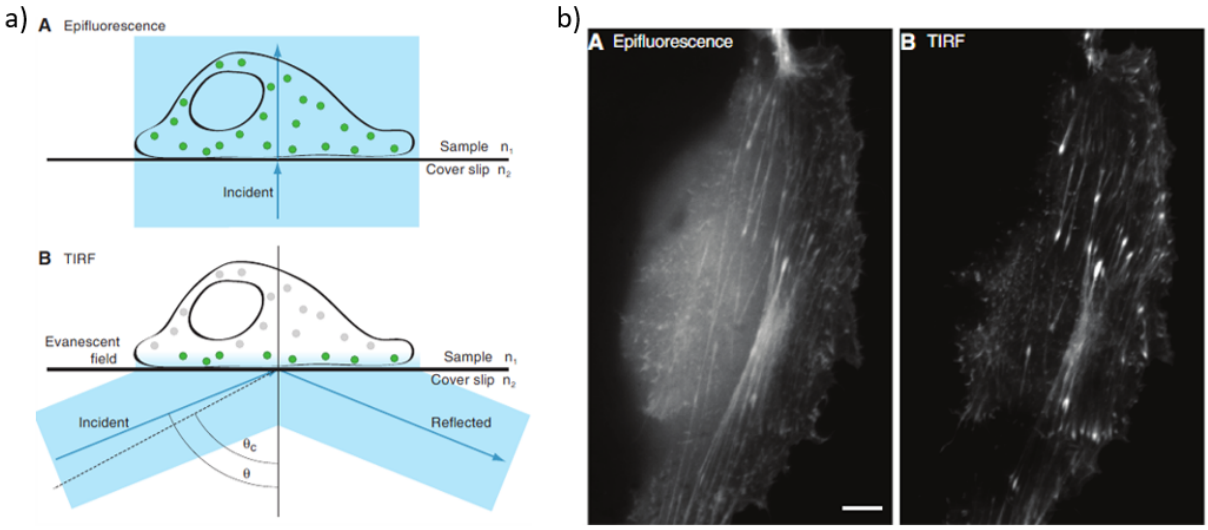

Figure 8: (a) The principle of epifluorescence and TIRF illumination [21]. (b) Fluorescence image of a migrating MDCK cell in epifluorescence and TIRF imaging modes [21].

2.2.2 STORM

A method to achieve resolutions that surpass the diffraction limit is Single Molecule Localization Microscopy (SMLM). Due to diffraction by the microscope objective, a single fluorophore emitting light will appear as a ∼200 nm-wide spot called the point-spread function (PSF). Such a spot is shown in Figure 9. When a fluorophore is well isolated, a Gaussian fit can be applied to localize the fluorophore with a spatial resolution of around 20 nm [22], [23].

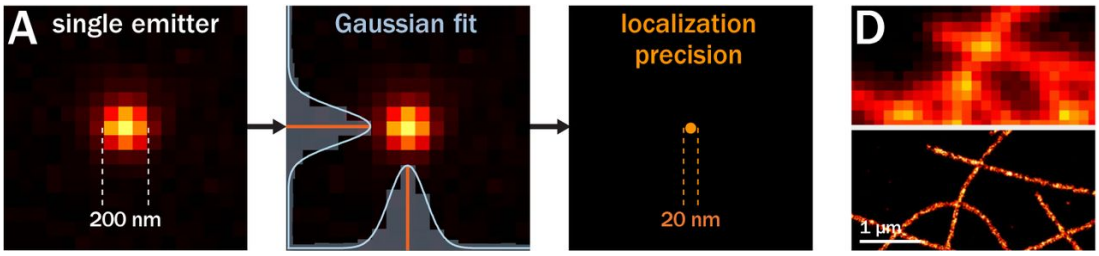

Figure 9: Schematic overview of localization in single-molecule localization microscopy [23].

However, fluorophores are often not well isolated. Stochastic Optical Reconstruction Microscopy (STORM) is a method that achieves these isolated fluorophores by using photoswitchable fluorescent dyes [22], [23]. The final image is constructed by combining a series of imaging cycles. In each cycle, a fraction of the fluorophores is switched on such that they are isolated. STORM achieves the blinking of fluorophores by switching them between a dark and a fluorescent state using light of different wavelengths. Only a few fluorophores switch to their fluorescent state when activated [22]. This allows the positioning of the fluorophores to be highly accurate. By repeating this cycle many times, the positions of many fluorophores are determined, and thus, an overall image can be constructed [22].

The high spatial resolution of STORM makes it ideal for capturing DNA origami structures. Another advantage of STORM is that it does not require complex optical systems, making it a more accessible option for super-resolution imaging [22].

Despite its strengths, STORM does come with several challenges. STORM is dependent on photoswitchable fluorophores, which can limit the variety of compatible dyes available for experiments. Moreover, this technique takes a long time to acquire due to the need for many localization cycles. Therefore, the method is unsuitable for fast-paced studies such as dynamics. The resolution quality also depends on factors like fluorophore density and the precision of molecular localization, and the resulting images can sometimes suffer from background noise, drift, or artifacts due to sparse labeling [22].

2.2.3 DNA-PAINT

DNA Point Accumulation for Imaging in Nanoscale Topography (DNA-PAINT) is a super-resolution imaging technique similar to STORM. The difference between the techniques is in how blinking is achieved. In DNA-PAINT, blinking is generated by the transient hybridization of a short DNA single-strand coupled to a fluorophore, called an imager strand, with its complementary strand (docking strand) [22], [24]. During hybridization, the fluorophore emits electrons until the unbinding. The constant binding and unbinding of the imager and docking strands are captured over time, thus resulting in an image of the structure [22]. An example signal and image of DNA-PAINT is shown in Figure 10.

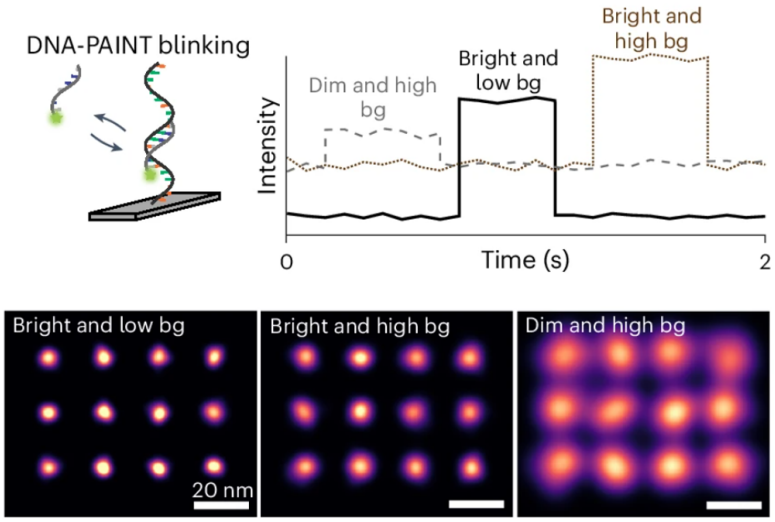

Figure 10: DNA-PAINT example signal with corresponding image [25].

One of the main strengths of DNA-PAINT is its spatial resolution of 10 nm [24]. The technique can reveal complex structures with high precision. Since the blinking relies on transient binding instead of illumination, DNA-PAINT suffers less from photobleaching. This results in longer imaging times and more consistent signal quality. Another advantage lies in the flexibility of using synthetic DNA strands as probes, which allows for customizable design and versatile labeling strategies.

Despite these advantages, DNA-PAINT has some disadvantages. The method requires the synthesis of short, complementary DNA strands. While not complex, it adds complexity to the measurements. Its reliance on transient binding may not be suitable for measurements requiring stable, long-term molecule interactions. Additionally, the technique requires a high signal-to-noise ratio for accurate fluorophore localization, which can be challenging to achieve in complex or crowded samples.

2.2.4 Fluorescence imaging techniques comparison

In Table 1, an overview of the advantages and disadvantages of FRET, STORM, and DNA-PAINT is shown. Based on the table, FRET is chosen to analyze the dynamic behavior of DNA origami nanopores. FRET is sensitive to small displacements and can show the dynamics in real-time. Therefore, FRET is chosen to analyze the dynamics.

Table 1: Comparison of fluorescence imaging techniques

Technique	**Advantages**	**Disadvantages**
FRET	High sensitivity to small distance changes, real-time monitoring, versatile	Requires close proximity of fluorophores, influenced by environmental factors, can be technically demanding
STORM	Achieves super-resolution imaging (20-30 nm), great detail, no need for complex equipment	Requires photoswitchable fluorophores, long acquisition times, possible background noise
DNA-PAINT	High resolution (10-20 nm), reduced photobleaching, flexible DNA probe design	Requires synthesis of DNA strands, transient binding may not be ideal for all studies, high signal-to-noise ratio needed

2.3 Immobilizing DNA origami structures

Immobilizing DNA origami structures is critical for many fluorescence applications. This is crucial for high-quality measurements because the structures will remain focused for extended periods rather than rapidly diffusing in and out of the illumination focus when untethered. This subsection gives an overview of two immobilization techniques that can be used to immobilize DNA origami structures.

2.3.1 Biotin-BSA

A standard method for immobilizing DNA origami structures is biotinylated bovine serum albumin (biotin-BSA). In this approach, the glass surface is passivated by a layer of biotin-BSA. Here, the BSA adsorbs to the surface, preventing adsorption of other molecules on the surface. At the same time, biotin acts as an anchor for streptavidin/neutravidin. DNA origami structures modified with biotin can then be introduced onto the streptavidin/neutravidin-coated surface [7]. Additionally, the method is modular. Therefore, it can be used for other biomolecules. A schematic overview of this process is shown in Figure 11.

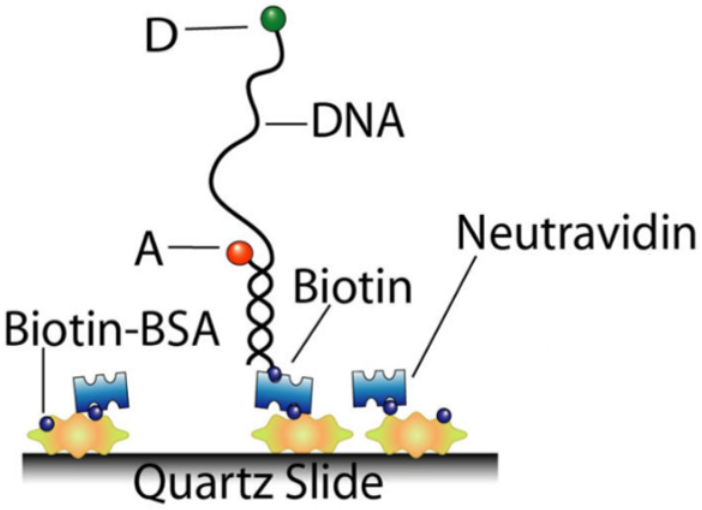

Figure 11: Schematic overview of biotin-BSA immobilizing a DNA origami structure [7].

2.3.2 Gold-thiol

Anchoring biomolecules onto gold surfaces is done through the gold-thiol (Au-S) bond. In the case of DNA origami structures, the strands are chemically modified to have a thiol group at the 5' or 3' end. When thiolated DNA is introduced onto a gold surface, the thiol groups form bonds with the gold. This technique is therefore simple and requires no intermediate layers.

To optimize surface passivation and prevent nonspecific adsorption, thiolated DNA is often immobilized in combination with short thiol-containing blocking agents, such as mercaptohexanol (MCH) or polyethylene glycol (PEG)-thiol. These molecules fill in the gaps between DNA strands on the gold surface, enhancing DNA accessibility and reducing background binding. The result is a clean, biologically active interface suitable for downstream applications such as hybridization, biosensing, or single-molecule fluorescence studies.

2.4 Nanoarray manufacturing

This subsection gives an overview of four different manufacturing techniques that can be used for manufacturing nanoarrays. The advantages and disadvantages of each technique are discussed. Eventually, a comparison is made between the methods.

2.4.1 Nanosphere lithography

A practical and economical method for creating nanoscale patterns on a surface is nanosphere lithography (NSL). This method uses a mono or multiple layers of nanospheres on a substrate. Often made of polystyrene or silica, nanospheres self-assemble into a hexagonal closed-packed (HCP) structure [13], [26]. A schematic overview of the self-assembled array is shown in Figure 12. The ordered arrays can then be used as material deposition or etching templates. By varying parameters such as sphere size or assembly method, NSL can produce size-tunable HCP structures without needing specialized cleanroom equipment and environment.

To fabricate these HCP structures, nanospheres are suspended in a liquid medium; this suspension is then applied to the substrate. As the solvent evaporates, the nanospheres self-assemble into an HCP structure due to capillary forces and convective nanosphere transport [13], [27]. The resulting monolayer can then be used as a mask for deposition or etching. The uncovered areas of the substrate determine the geometry of the final nanostructure.

A second method for forming nanosphere monolayers is with spin coating. During this process, a droplet of the nanosphere suspension is placed on the substrate. The substrate is then rapidly spun; the centrifugal forces spread the nanospheres evenly across the surface. At the same time, the solvent evaporates, leaving behind a self-assembled monolayer of nanospheres. Parameters such as spin speed, nanosphere concentration, and solvent

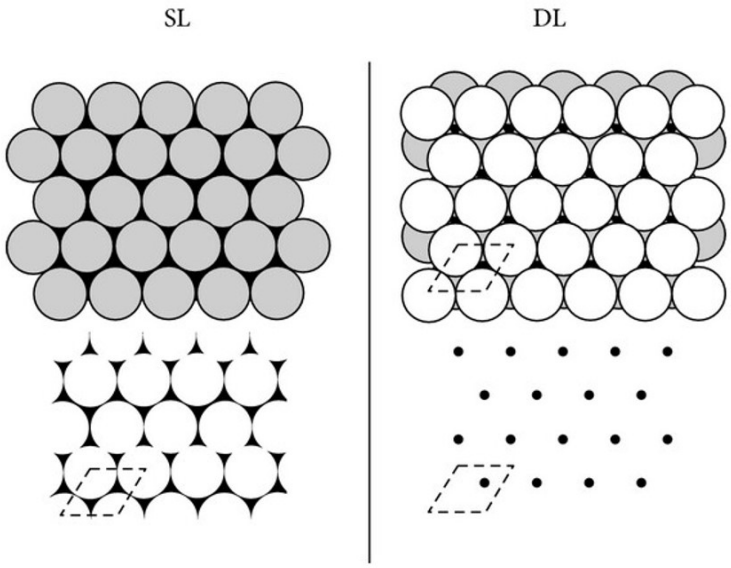

Figure 12: Schematic diagrams of mono/single layer (SL) and double layer (DL) [26].

properties affect the final arrangement of the nanospheres [27]. The advantage of spin coating is that the method is reproducible and can cover large, flat surfaces.

The air-water interface method is another approach to assembling nanosphere monolayers. A droplet of the nanosphere suspension is spread over the surface of a water bath. The nanospheres then migrate to the air-water interface, forming an HCP monolayer due to surface tension and capillary forces. The floating monolayer is transferred onto a substrate by carefully lifting it through the water surface. The main advantage of this technique is that it can place a monolayer on substrates with complex geometries [27].

However, NSL has some disadvantages. While its resolution depends on the nanosphere size, NSL is limited to HCP structures. More complex or varying geometries cannot be manufactured using NSL. Furthermore, the self-assembled structures are prone to defects, which can result in local areas without arrays.

2.4.2 Soft Lithography

Soft lithography is a commonly used technique to create micro- and nanoscale patterns on various substrates, especially for microfluidics, biosensing, and nanotechnology applications. This technique utilizes flexible molds made from elastomeric materials, such as polydimethylsiloxane (PDMS), which replicate patterns on a substrate [28], [29]. The process starts with creating a master mold, often made by photolithography or other high-resolution techniques. Then, an elastomer is cast over the master mold; this is peeled away once cured. This results in a transfer of the pattern to the target substrate [28]. A schematic overview of the process is shown in Figure 13. The substrate's material can vary from glass to plastics or metals [28].

Soft lithography is a low-cost fabrication method that uses simple, inexpensive materials and tools [28], [29]. No expensive photomasks or complex equipment are required. Additionally, the process is scalable, meaning it can be used for small or large-volume production.

However, soft lithography has its limitations. The resolution is generally in the range of tens of nanometers. This is relatively high when compared to techniques like e-beam lithography [28]. Moreover, the master mold will experience wear and degradation when subjected to repeated use. This will, over time, affect the quality of the prints and thus limit the long-term viability of the technique for high-precision and throughput applications.

2.4.3 E-Beam Lithography

E-beam lithography (electron beam lithography) is a high-resolution technique that creates nanoscale patterns on various substrates. This technique uses a beam of electrons to write patterns onto a surface coated with an electron-sensitive resistor material [28], [31]. The interaction between electrons and the resistive layer activates a chemical change, allowing selective pattern etching. E-beam lithography is used for the fabrication of devices

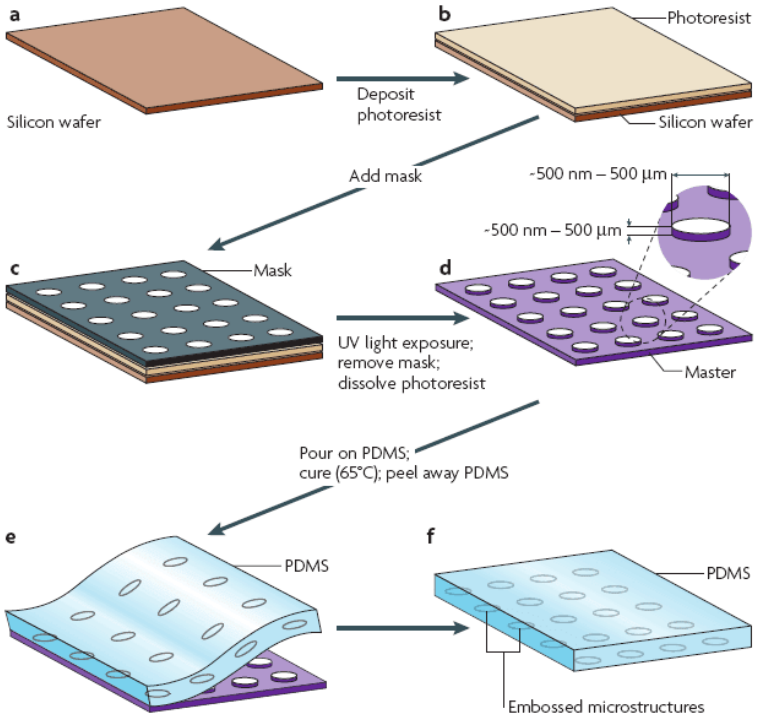

Figure 13: Schematic overview of soft lithography [30].

where a high resolution is required. Examples are semiconductors, quantum dots, and other nanostructures [28], [31].

The main advantage of e-beam lithography is its sub-10 nm resolution [28], [31]. This allows for fabricating detailed patterns in developing nanotechnology, photonics, and semiconductor manufacturing. Moreover, the technique is highly flexible, allowing users to create custom patterns without needing masks or photomasks, which are costly and time-consuming [28], [31].

However, e-beam lithography comes with several limitations. The process is slow since it manipulates one pixel at a time. Mask-based photolithography techniques, on the other hand, can expose an entire wafer simultaneously [28], [31]. Therefore, e-beam lithography is not suitable for large-scale production. Additionally, the equipment for e-beam lithography is specialized and expensive, contributing to its high cost. Finally, despite its high resolution, it remains possible that electron scattering can contribute to defects or artifacts [28].

2.4.4 Focused Ion Beam Lithography

Focused ion beam (FIB) lithography is a direct-write technique that uses a highly focused beam of ions, usually gallium, to write or mill patterns onto a substrate [28], [32]. The ion beam interacts with the material, causing it to either etch away or deposit new material, depending on the desired outcome [28], [32]. This allows for patterning on various materials, including metals, semiconductors, and insulators.

One of the key advantages of FIB lithography is its high resolution. Furthermore, the ability to etch or deposit materials makes FIB useful for rapid prototyping or modifying existing structures. Since FIB is a direct-write method, it eliminates the need for photomasks or masks completely, which reduces setup time and costs in some applications [28].

Like e-beam lithography, FIB is slow and an unsuitable process for large-scale production. This makes it less practical for high-throughput manufacturing environments. Another disadvantage is that high-energy ions can cause damage to the substrate. Like roughness around the patterns [28]. Additionally, the cost of FIB equipment is high, and skilled operators are required to ensure precise patterning, which adds to the total cost of the technique.

2.4.5 Nanoarray fabrication techniques comparison

In Table 2, an overview of the advantages and disadvantages of NSL, soft lithography, E-beam, and FIB lithography is shown. Based on the table, NSL was chosen to fabricate nanoarrays. NSL is cost-effective and straightforward, making it accessible to many researchers. Its main strength for this project is that after the nanospheres have been self-assembled, many other materials can be deposited to create binding spots in the unaffected areas. While soft lithography could achieve the same, the need for a master mold makes it more complicated than NSL.

Table 2: Comparison of nanoarray fabrication techniques (10-1000 nm resolution)

Technique	**Resolution**	**Cost**	**Pattern Flexibility**	**Advantages**	**Disadvantages**
Nanosphere Lithography	100-1000 nm	Low	Limited	Cost-effective, self-assembly, scalable	Limited pattern variety, defect-prone assembly
Soft Lithography	>15 nm	Low	Moderate	Flexible molds, low-cost	Limited resolution, mold degradation over time
E-Beam Lithography	<10 nm	High	High	High resolution, precise pattern control, complex designs	Expensive, slow process, limited scalability
Focused Ion Beam Lithography	<10 nm	High	High	High precision, direct-write capability, no need for masks	High cost, time-consuming

3 Research proposal

3.1 State of the art

The placement of a DNA origami structure within a nanoarray has been previously studied. However, the goal of these papers was not to improve FRET signals. The paper from Gopinath et al. created binding spots for direct self-assembly of DNA origami structures for coupling molecular emitters to photonic crystal cavities [33]. Furthermore, binding spots shaped as the DNA origami have been fabricated [11], [12]. These two papers have achieved their goal successfully. The downside of these three papers is that they used costly e-beam techniques.

There is limited to no literature that mentions cheaper methods for fabricating arrays or using them to improve FRET measurements. However, one paper by Shetty et al. proposes using a nanoarray to improve FRET while being cost-effective [13]. Many findings and ideas of this research are based on this paper.

The paper mentions that bulk FRET measurements encounter problems with samples overlapping within the diffraction-limited spot due to the stochastic nature of surface-immobilizing DNA origami structures. The paper discusses increasing the measurement throughput by placing the DNA origami structures in a nanoarray. This will solve the problem of overlapping samples and potentially improve the FRET signals. In Figure 14, a nanoarray is schematically shown to increase the throughput for characterizing DNA origami structures. Shetty (2021) uses NSL as a cost-effective method to fabricate a nanoarray and then discusses how they successfully placed DNA origami structures in the array.

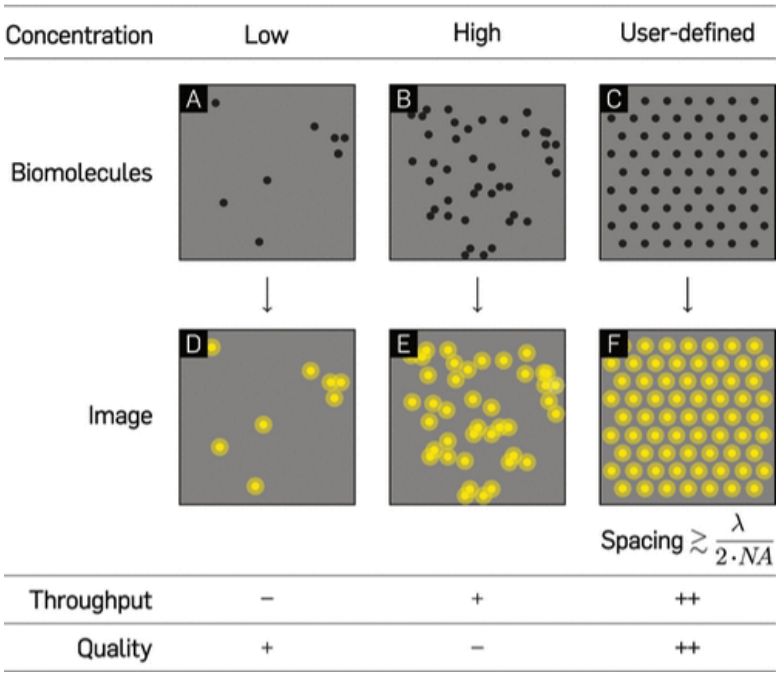

Figure 14: Comparison between unpatterned and patterned experiments [13]

However, improvements can be made to their methodology. For example, they use toxic chemicals during the fabrication process. The chemicals are harmful to the environment; thus, there is a need for a method that uses non-toxic chemicals.

3.2 Research gap

DNA origami actuators are proposed as size-adjustable DNA origami nanopores. SEM or DNA-PAINT is often used to characterize the different states of these actuators. Some example papers are shown in Table 3. While the structures have distinct shapes, it makes sense to use those techniques. Furthermore, they offer higher resolution and can show a more direct view of the structure. However, the rapid dynamics cannot be seen with these techniques. Knowing the rapid dynamics can be helpful for applications like targeted drug delivery. Studying the rapid dynamics ensures a precise and controlled release of therapeutic agents at the right time and place.

Fluorescence imaging is done in bulk. From the papers presented in Table 3, it can be seen that the random surface immobilization of the DNA origami structures can result in closely overlapping samples and, thus, data loss. Lowering the origami concentration would solve this problem; however, the data throughput would be lower. For easier analysis, it is essential that the imaging can be done with high throughput. A method to achieve this would be placing the DNA origami structures within nanoarrays. However, no dynamic DNA origami structure has been placed within these arrays. Thus, there is a need to study the placement of a dynamic DNA origami structure within a nanoarray.

Table 3: State-of-the-art sources

Papers showing overlap in structures placed for FRET analysis	[13], [34], [35]

3.3 Research question and objectives

Based on the research gap, the research question of this master's thesis is: How can nanoarrays improve the data quality from FRET measurements of DNA origami structures? To address the research question, three objectives are formulated:

- Produce with 95% confidence nanoarrays with at least 5x5 binding spots and with varying spacing while using non-toxic chemicals.
- Immobilize DNA origami structures on at least 50% of the available binding spots in the nanoarray with a 95% confidence interval.
- Compare the dynamics of DNA origami structures when placed within the nanoarray with randomly placed ones, showing no significant difference in dynamics.

A better understanding of NSL is required to achieve consistent and predictable nanoarrays. Without relying on toxic chemicals, the proposed method will become more accessible for other researchers to implement while being better for the environment. Furthermore, FRET analysis with TIRF microscopes requires immobilizing DNA origami structures. Therefore, the two proposed arrays of reduced sphere size and gold islands should achieve this without altering the dynamics of DNA origami structures.

The first subobjective will be achieved by manufacturing both types of nanoarrays. 300, 600, and 800 nm nanospheres will be used to vary the spacing. Furthermore, the impact of oxygen plasma exposure on the nanoarray will be analyzed. Here, SEM and AFM will be used to characterise the mask and nanoarrays. This data will be analysed using statistics across different samples that undergo the same treatment for statistical significance.

Since there are two different types of nanoarrays, both methods will be used to achieve the second subobjective. DNA origami structures will be immobilized on the non-exposed glass surface for the reduced sphere size nanoarray. This will be achieved with biotin-BSA as a coupler between glass and DNA origami structures. The gold islands nanoarray will use thioled DNA origami structures. These structures self-assemble onto the gold nanoarray. Fluorescence measurements will be performed to validate the performance of these methods. These measurements will reveal how well the DNA origami structures immobilize within the nanoarray. Finally, the data collected during these experiments will also be used to determine if the third objective has been achieved.

4 Methodology

This section overviews the protocols used for sample preparation and the experiments. Furthermore, details about the experimental setup are given, including the equipment used and its settings.

4.1 Nanofabrication techniques

This subsection provides two fabrication techniques used during the manufacturing of the nanoarrays. These techniques were used to simplify the entire manufacturing procedure, enabling researchers with non-specialised equipment to use nanoarrays for their experiments.

4.1.1 Sputter coater

A basic sputter process takes place in a vacuum. Here, a target plate is bombarded by ions generated in a glow discharge plasma in front of the target surface [36]. The bombardment results in the removal (sputtering) of the target atoms, which then condense onto a substrate, forming a thin film. To improve the efficiency of this process, magnetron sputtering was developed, using a magnetic field. Here, the ion bombardment's secondary electrons are contained within this field. This increases the chances of electron-atom collisions, leading to a denser plasma and thus higher ion bombardment, giving a higher sputtering rate [36].

4.1.2 Oxygen plasma cleaning

Oxygen plasma cleaning is a surface modification technique where oxygen gas is ionized in a vacuum to form plasma. The advantages of the cleaning are that it removes inorganic matter or increases surface wettability. An alternating electric field energizes oxygen gas to form plasma. The plasma, composed of ions and electrons, then interacts with the surface through bombardment and chemical reactions. In the context of this project, oxygen plasma is used to etch nanospheres. This reduces their size in a controlled manner. The extent of material removal can be controlled by varying parameters such as exposure time, power, and gas flow rate.

4.2 Flowcell preparation

Four protocols are described below: 1) nanosphere suspension preparation, 2) gold nanoarrays manufacturing, both the reduced sphere size and the gold islands method, 3) DNA origami folding, and 4) flowcell assembly.

4.2.1 Nanosphere suspension preparation

These steps are followed to obtain the suspension for the nanospheres used during NSL:

- In an Eppendorf tube, 100 μL suspension of 300 nm, 600 nm, or 800 nm PS nanospheres was poured and vortexed before use.
- The tube was spun at 10,000 rpm for 5 min.
- The supernatant was removed, and 150 L of ultrapure water was added to resuspend the nanospheres. The spin process at 10,000 rpm for 5 min was repeated.
- Finally, the supernatant was removed, and the nanospheres were resuspended in a 30% ethanol and 70% water solution of 100 μL.
- The tube was vortexed to resuspend all nanospheres and prevent agglomeration.

4.2.2 Nanoarray, reduced sphere size

These steps are followed to create a gold nanoarray that will create binding sites for DNA origami structures to bind to:

- A cover slip was cleaned by sonication in IPA and acetone for two minutes, respectively.
- The cover slip was cleaned by 10 min of oxygen plasma exposure. This step removes residual contamination and makes the glass surface more wettable.
- 10 μL of the nanosphere solution is drop-cast on the glass surface. Then the glass is put under a 45-degree angle for the solution to dry.

- The glass was heated at 60 °C for a few minutes to remove moisture from the sample.
- OPTIONAL extra oxygen plasma exposure for 2-10 min to reduce the bead size while keeping the spacing.
- With a gold sputter coater, a 40 nm gold layer is deposited on the sample. This created the gold array.
- The nanospheres were removed in ultra-pure water using an ultrasonic cleaner.

4.3 Nanoarray, gold islands

These steps are followed to create a gold nanoarray that will create binding sites for DNA origami structures to bind to. The starting steps are the same as for the reduced sphere size protocol. Starting from the optional step, the following protocol is used:

- An aluminum block was heated up to 107 °C. The glass is then placed on the block for 20 seconds to melt the nanospheres partially
- With a gold sputter coater, a 40 nm gold layer is deposited on the sample. This created the gold array.
- The nanospheres were removed in toluene using an ultrasonic cleaner for 2 min.
- The glass is rinsed and dried twice with ethanol and a nitrogen gun.

4.3.1 DNA origami folding

The FRET rulers and HJs were thermally annealed with the same procedure. The sample was heated to 90 °C with an incubation time of 5 min. Then the mixture was rapidly cooled to 65 °C for 5 min. Then the sample was slowly heated again to 90 °C over 2 hours. For the gold islands nanoarray, a thiol modification is used in the oligos instead of a biotin modification.

4.3.2 Flowcell assembly

These steps were followed to bind DNA origami samples in the reduced sphere size nanoarray:

- A microscope slide was cleaned by sonication in IPA and acetone for two minutes.
- The flow chamber was assembled using a microscope slide, modified cover glass with the array, and double-sided tape.
- 80μL of BSA-biotin (1 mg/mL, dissolved in buffer A) was incubated for 5 min, followed by washing of the channels with 450 μL buffer A.
- 100 μL of neutravidin (0.5 mg/mL in buffer A) was added to the channels for 5 min, and then the sample was washed first with 150 L of buffer A and then with 450 μL of buffer B.
- DNA origami equipped with biotin was incubated in the channels for 5 min, then washed with 450 μL of buffer C.
- The chamber was sealed off with two-component epoxy glue.

Buffer A: 10 mM Tris pH 8, 100 mM NaCl, and 0.05% Tween-20.

Buffer B: 10 mM MgCl2, 5 mM Tris-HCl pH 8, 1 mM EDTA and 0.05% Tween-20, pH 8.

Buffer C: 10 mM MgCl2, 5 mM Tris-HCl pH 8, 1 mM EDTA and 0.05% Tween-20, pH 8, 10mM PCA, 10mM PCD, 10mM TROLOX.

The flowcell construction for the gold islands nanoarray was very similar. A channel was created between a microscope slide, a cover glass with an array, and double-sided tape. The thiol-modified DNA origami structures were introduced to the chamber in buffer C. While incubating, the chamber was sealed off with two-component epoxy glue.

4.4 Experimental setup

This subsection gives an overview of the equipment used, its specifications, and settings.

4.4.1 Oxygen plasma cleaner

The plasma cleaner used was a Diener Femto plasma cleaner. All procedures were performed at 100% power, which equals 100 watts for the preselected time. The following procedure was used to operate the machine:

- Pump to 0.10-0.16 mbar.
- Let the oxygen in at a 5-6 sccm rate.
- Pump to 0.10-0.16 mbar.
- Oxygen plasma exposure for the set time.

4.4.2 Gold sputter coater

The gold sputter coater used was a JEOL JFC-1300 auto fine coater. It used a planar magnetron sputter target configuration for efficient, high-rate sputtering with minimal specimen heating. The machine was operating at a current of 20 mA. The specimens were placed at a fixed distance of 25 mm. This results in a deposition rate of 0.67 nm/s.

The sputter coater used an automatic cycle:

- Pump to 0.05 mbar.
- Flush for 3 sec with argon.
- Pump to 0.15 mbar.
- Flush for 3 sec with argon.
- Pump to 0.05 mbar.
- Switch on the sputter supply at the preselected current.
- Switch off the sputter supply after the preselected time.

4.4.3 TIRF Microscope and laser

A TIRF microscope was used for fluorescence imaging to minimize background noise, and the DNA origami structures were closely immobilized at the surface. The nanopore will be labeled with Cy3 and ATTO647N for donor and acceptor, respectively. Cy3 is chosen for its strong fluorescence, while ATTO647N is chosen for its brightness and photostability.

The microscope was a Nikon Eclipse Ti-2 with a 100× oil immersion objective and Photometrics Kinetix sCMOS sensor. The microscope was operated with Nikon NIS software. The laser was a 10 mW class 3 operating at 470 nm, 532 nm, and 640 nm wavelengths.

4.4.4 AFM

Atomic Force Microscopy (AFM) is a powerful tool for capturing high-resolution images of material surfaces at the nanoscale. AFM creates three-dimensional maps of surface features by moving a sharp probe across the sample's surface and detecting the forces that arise from their interaction [37]. With different operational modes, such as contact, non-contact, and tapping, it can adapt to various environments, including air, liquids, and vacuum, making it highly versatile for different applications. A schematic overview of the working principle of an AFM is shown in Figure 15.

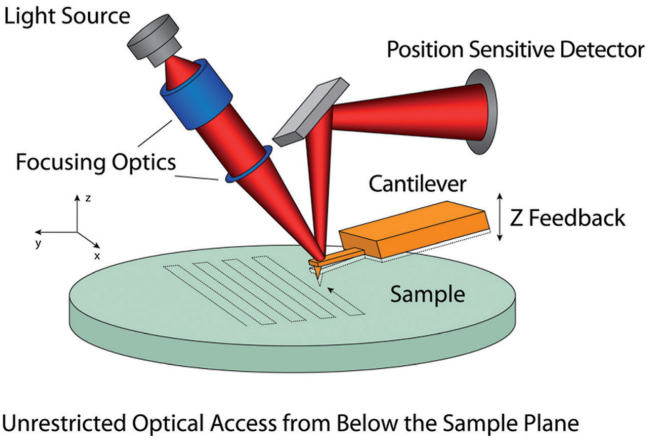

Figure 15: Schematic overview of working principle AFM [37].

By moving the tip across the sample's surface, the atoms of the tip receive an attraction or repulsive force. This depends on the distance between the tip and the sample. The received forces affect the height of the cantilever; this height is detectable by a position-sensitive detector. The sensor's light change can then be related to a height profile.

The AFM used was a Nanosurf Nanite B in tapping mode with an NCLR tip. In contact mode, the AFM tip may displace any features on the surface; therefore, tapping mode was used. The AFM then collected data about the morphology of the structure. This was used to relate nanosphere size to binding spot size and more.

4.4.5 SEM

Scanning Electron Microscopy (SEM) is a technique for capturing detailed images of a material's surface. It works by directing a focused beam of electrons onto the sample. As the electrons interact with the atoms in the material, they release secondary electrons that are detected to form an image [38]. This process reveals the sample's surface morphology, texture, and composition. SEM offers magnifications ranging from 10x to several hundred thousand times, allowing for visualization at the nanoscale. One limitation, however, is that non-conductive samples require a thin conductive coating to prevent image distortion.

The JEOL 6010LA was used for SEM with a tungsten filament as the electron source. The SEM operated in the SEI mode; carbon tape was used to increase the conduction between the sample and the sample holder. The electrons were accelerated at 15-20kV.

SEM was used to image the fabricated nanoarray. Firstly, the surface with the nanospheres still attached will be analyzed. This will give an insight into how well the nanospheres are self-assembled into an HCP structure and show any defects within the array. Afterward, the nanoarray with a binding spot can be analyzed using SEM. Compared to AFM, larger areas can be imaged within a shorter period. This makes SEM helpful in seeing how well NSL is performed.

5 Results

This section presents the results from the fabrication and characterization of nanoarrays and fluorescence measurements. The section consists of two subsections; the first focuses on the nanoarray, and the second on the fluorescence measurements and the dynamics of the DNA origami structures.

5.1 Generation and characterization of nanoarrays

The initial steps for manufacturing the nanoarray were based on the protocol from Shetty et al [13]. However, two problems were found with their protocol. Firstly, the difference in nanosphere concentration in their original suspension resulted in a very viscous ethanol/water/nanosphere solution. Therefore, it was not easy to control and predict the behaviour of the solution while depositing it on glass. Secondly, the self-assembled monolayer of nanospheres did not adequately cover the glass surface. There were limited regions with large areas of monolayers, and most of the surface had small monolayers. It is preferred that the nanospheres cover most of the glass surface. This will make the nanoarray characterization and fluorescence measurement more statistically significant. Two images of a coverslip with a high-quality nanosphere mask are shown in Figure 16.

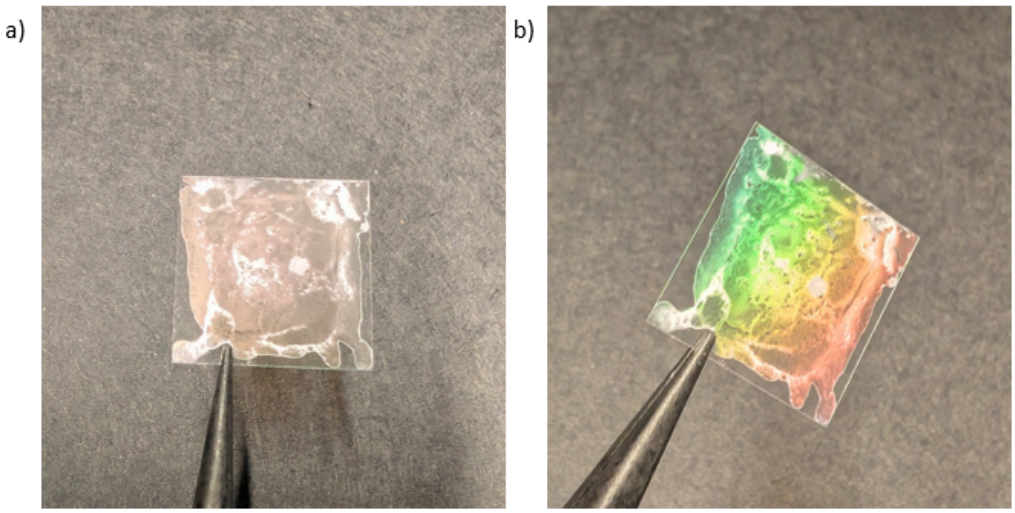

Figure 16: (a) Cover slip glass with an evenly distributed nanosphere mask 600 nm nanospheres. (b) Under an angle, the masks light up as a rainbow, indicating a monolayer's presence.

Experimentally, it was found that reducing the nanosphere concentration by a factor of ten resulted in an ideal solution. Furthermore, instead of dropcasting, spin coating was introduced to improve monolayer uniformity and coverage. A comparison between drop casting with drying under a 45° angle and spin coating at 350 rpm (50 rpm/s acceleration) for 1 minute with immediate drying at 60° for 5 min is shown in Figure 17. The observed color difference indicates a variation in light reflection: yellow/green areas represent a lack of nanospheres, dark brown areas represent a monolayer. In contrast, the other colors indicate multilayered regions.

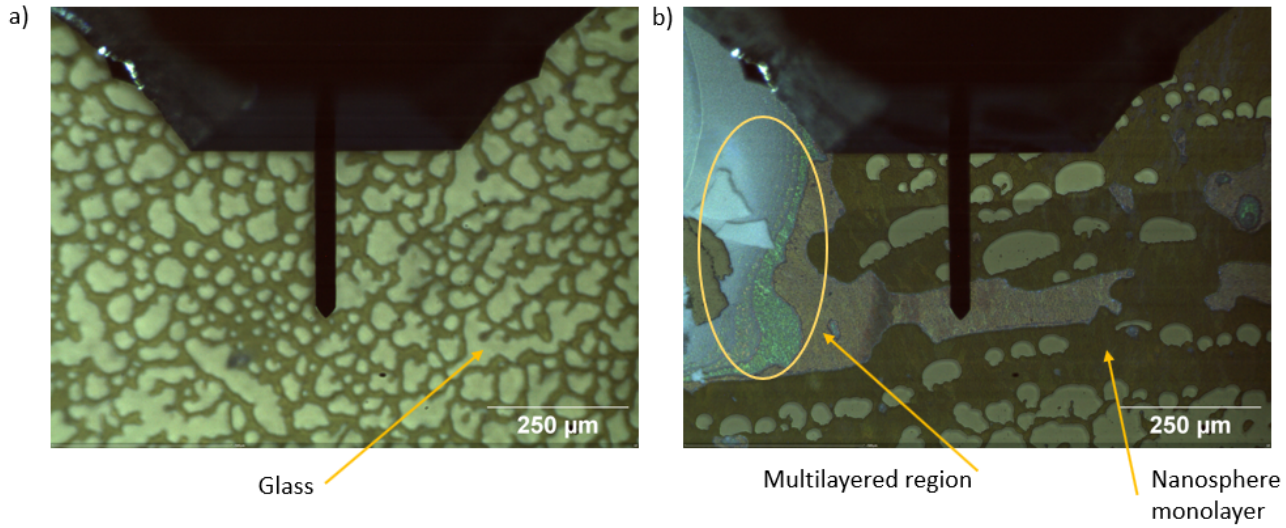

Figure 17: (a) Glass surface after drop coating with 600 nm nanospheres. (b) Glass surface after spin coating at 350 rpm for 1 minute with 600 nm nanospheres.

The nanospheres act as a mask for NSL, and arrays are achieved by depositing a metal on the nanospheres. A gold sputter coater was used to deposit a 40 nm thick gold layer. Afterwards, the nanospheres were removed from the surface by sonication in water for 1 minute, revealing the underlying nanoarray. AFM images of arrays produced using 600 nm and 800 nm nanospheres are shown in Figure 18a and Figure 19a. The figures show that the contact area between the nanosphere and glass (dark brown) can be distinguished from the deposited gold structure (red). In addition, the spacing between the non-exposed regions is shown in Figure 18b. The spacing here, around 600 nm, corresponds to the nanosphere size. Additionally, from the figures, it can be said that the proposed method of reduced sphere size arrays can achieve the 5x5 binding spot criteria easily.

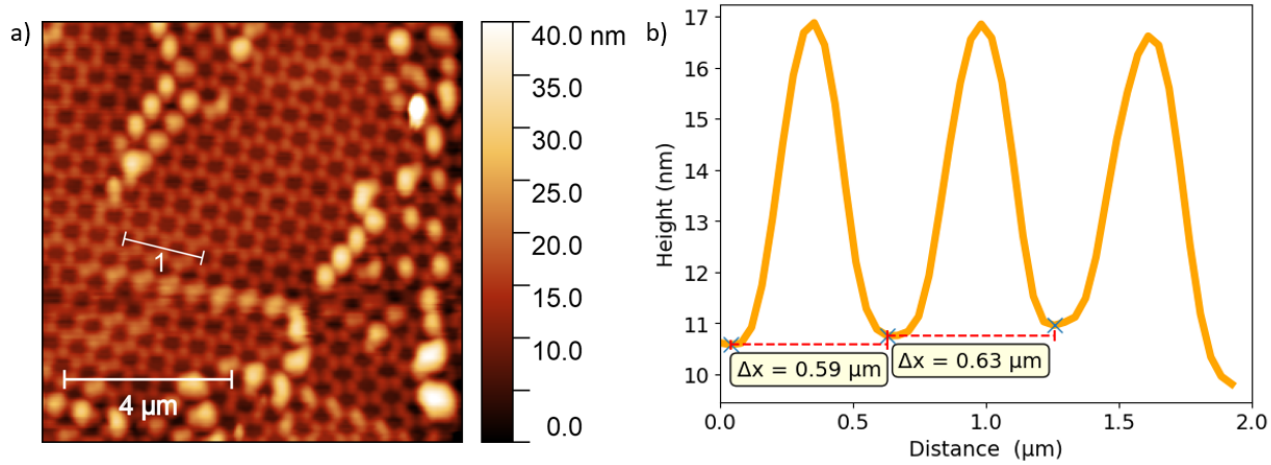

Figure 18: (a) AFM image of a nanoarray with a 600 nm nanosphere mask. (b) Line profile showing spacing between non-exposed areas.

Although generally successful, some imperfections were observed. For example, in Figure 19a, at the bottom, there is an elevated region compared to its surroundings. Furthermore, in both Figure 18a and Figure 19a, random, thicker spots are visible (bright yellow/white). Defects in the nanosphere mask cause these imperfections. These defects are visualized in Figure 19b. Excess gold gets more easily deposited in the gaps if the nanospheres are not perfectly arranged in an HCP structure, resulting in locally higher structures.

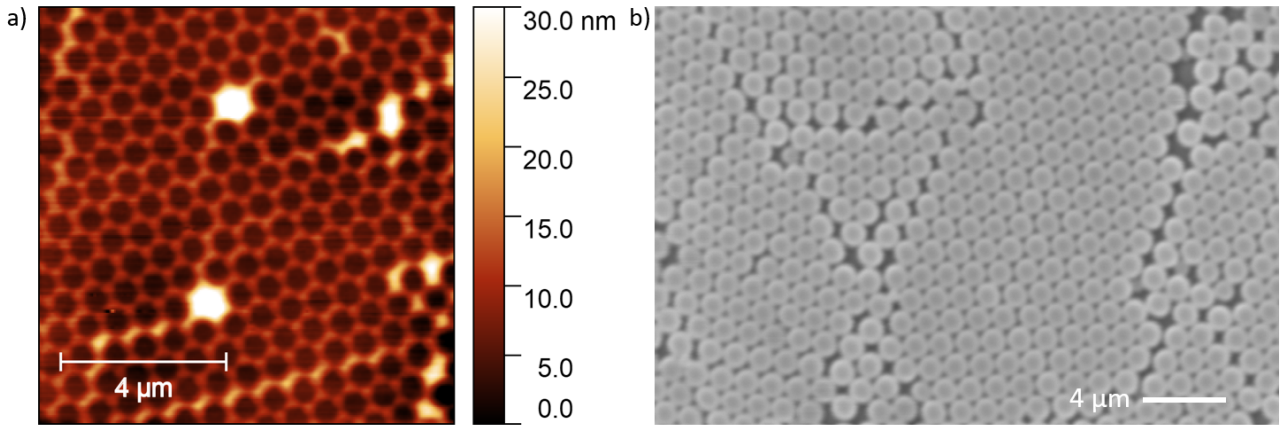

Figure 19: (a) AFM image of a nanoarray with an 800 nm nanosphere mask. (b) SEM image of a nanosphere monolayer with defects at 8,500x magnification. Imaging setting; SEI, 15 kV, WD27mmSS53

While the defects may affect the overall quality of the nanoarray, regions with an intact HCP remain consistent in their spacing and size. This consistency can be seen in Figure 20. The line profiles show periodicity and consistent spacing of the nanoarray in two directions. Therefore, it can be said that NSL can be used to create a consistent repeating structure. The reduction of defects has not been investigated since the quality of the nanoarray will be satisfactory for the rest of the project.

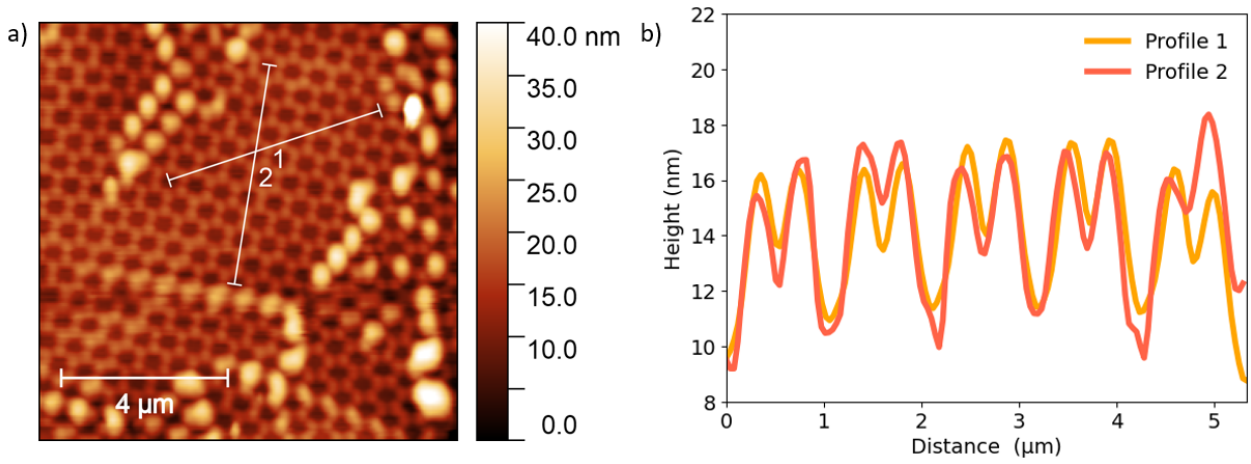

Figure 20: (a) AFM image of a nanoarray with a 600 nm nanosphere mask. (b) Line profiles showing the consistency of the array in two directions.

5.1.1 Reducing sphere size via oxygen plasma exposure

To successfully immobilize single DNA origami structures in an array, the binding spot should only allow for the binding of one structure. When looking back at Figure 18a, the binding spot size can be estimated to be around 400 nm, while the DNA origami structures are significantly smaller (around 10-100 nm). The binding spot size must be reduced to minimize the possibility of multiple origami structures being on the same binding spot. Therefore, controlled size reduction of the nanospheres is required to achieve this. Oxygen plasma exposure was used to reduce the nanospheres' size by etching the mask before gold sputtering.

The size of the binding spot is determined for nanoarrays fabricated using 300, 600, and 800 nm nanospheres exposed to 0, 5, and 10 min of oxygen plasma. A custom Python script (based on Isabelle Block's script, MSc) was used to analyze the AFM image of the nanoarray. The code uses the scale bar of the image and converts it to a nm/pixel value. Based on the contrast, the contour of shapes can be extracted from the image. The number of pixels inside this contour can be converted to a circle with the same pixels and thus area; the circle's diameter was used to find the effect of oxygen plasma exposure on the nanospheres. Furthermore, the code looped for different thresholds (to create a binary image with the contours) and window sizes (to find the edges)

to estimate the contours better. The circles' diameters were only allowed to be within a given range, which also helped filter out noise manually. Eventually, the result with the most circles while satisfying $mean/std = 0.1$ was given. 0.1 was chosen since it reduced the spread in data, while not overfitting the data. In the worst-case scenario, the 95% confidence interval would be $mean \pm 1.96 * std = mean \pm 0.196 * mean$, which seems reasonable. An example for 600 nm after 5 min of oxygen plasma exposure is given in Figure 21. In Table 4, an overview of the 95% confidence interval for binding spot diameter is given after oxygen plasma exposure for different nanosphere sizes..

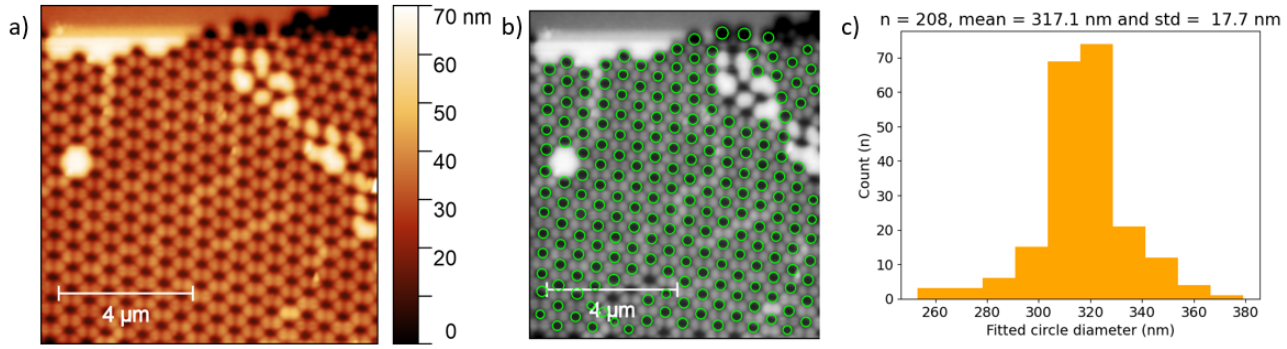

Figure 21: Example of analysis binding spot size for 600 nm nanospheres after 5 min of oxygen plasma exposure. (a) AFM image surface. (b) Fitted circles on the binding spot. (c) Histogram of circle diameter.

Table 4: Overview of 95% confidence interval for binding spot diameter for different oxygen plasma exposure times

Nanosphere/Exposure	0 min	5 min	10 min
300 nm	191.1±37.2 nm	195.2±38.0 nm	119.5±18.2 nm
600 nm	381.3±28.8 nm	332.3±45.7 nm	295.8±50.8 nm
800 nm	523.6±44.9 nm	470.8±55.9 nm	423.2±59.6 nm

Figure 22a shows an overview of AFM images illustrating all combinations of nanosphere sizes and oxygen plasma exposure times scaled for visual comparison. From the figure, it can be seen that the binding spot, particularly for the smallest bead size, decreases as the oxygen plasma time is increased. Furthermore, the mean binding spot diameter is normalized and plotted in Figure 22b. For the three different bead sizes, similar behaviour was found after oxygen plasma exposure for the binding spot size. The average decrease of spot size diameter was 8% after 5 min, and 26% after 10 min of plasma exposure time.

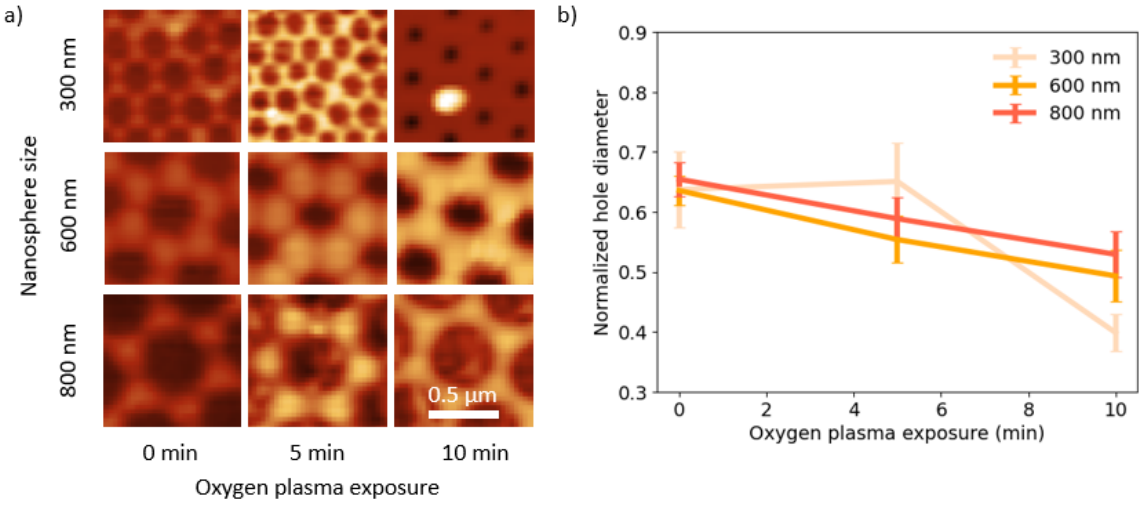

Figure 22: (a) AFM images of nanoarray structures for different nanospheres after oxygen plasma exposure. (b) Normalized binding spot size for different nanospheres after oxygen plasma exposure.

However, the accuracy of the analysis can be improved. The values and errors give a good estimation for the order of magnitude of the binding spot size. Still, the results are susceptible to the user input of the allowed circle diameter size. In the analysis shown in Figure 21, the allowed circle range was between 250 and 400 nm. This range was chosen for its high peak in the standard distribution in the middle of the range. All samples for 600 nm nanospheres after 5 min of oxygen plasma exposure were also analysed within the same range for consistency and gave similar results. However, a smaller mean binding spot size was found by changing the circle range to be between 250 and 350 nm. These results are shown in Figure 23. Based on the fitted circle image, the circles still cover the entire binding spot. Moreover, the histogram also shows a precise normal distribution with a slightly smaller peak in the middle. Therefore, by manually configuring the circle range, the results could change and thus affect the accuracy of the analysis. The results presented in Table 4 summarize the ranges that are deemed most representative.

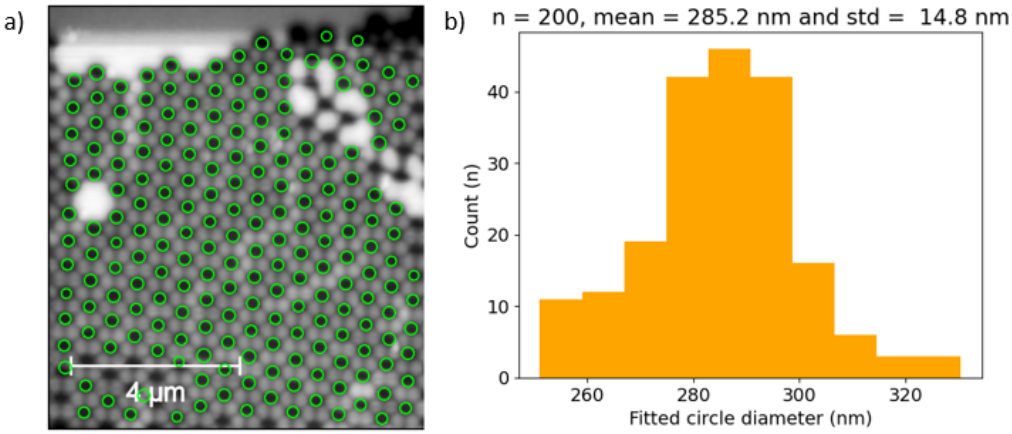

Figure 23: Binding spot size analyses for 600 nm nanospheres after 5 min of oxygen plasma exposure with a range of 250 to 350 nm circle size. (a) Fitted circles on the binding spots. (b) Histogram of circle diameter.

Furthermore, in Figure 22 for the 300 nm nanospheres, after 10 min of oxygen plasma exposure, a single nanosphere is still present in the figure. On the sample's surface, more nanospheres remained attached after sonication. Due to the smaller nanosphere size, the gold sputtering resulted in the encapsulation of the nanospheres. This problem occurred less prevalently for the 600 nm nanospheres after 10 min of oxygen plasma exposure. To solve this, sonication was performed for 1-2 min in toluene to remove these remaining nanospheres. After sonication, the sample was rinsed and dried twice with ethanol and a nitrogen gas gun. Toluene is a toxic substance and is ideally not used in the fabrication process. However, longer sonication or sonication in acetone did not solve the problem of the nanospheres remaining attached to the surface. Other alternatives were not explored during this project due to time constraints. Therefore, I decided to keep using toluene as a solvent to remove the nanosphere mask from the glass substrate.

Besides the change in binding spot size, the nanoarrays' height and morphology are also affected by oxygen plasma exposure. These changes are visualized in Figure 24. Five circular line profiles with 100 data points were normalized and averaged around a binding spot. The absolute height would be arbitrary, since it is based on the AFM image color intensity, and therefore it is chosen to be normalized with the maximum value of each profile corresponding to 1. It can be seen that without oxygen plasma exposure, there is a periodic height pattern; the amplitude of the pattern is increased after 5 minutes of oxygen plasma exposure. However, the amplitude is lower after 10 minutes of oxygen plasma exposure than without. This is due to the further etching of the nanosphere mask. It has almost reached a point where the gaps between the spheres are small enough not to block the gold deposition, resulting in a more uniform height profile.

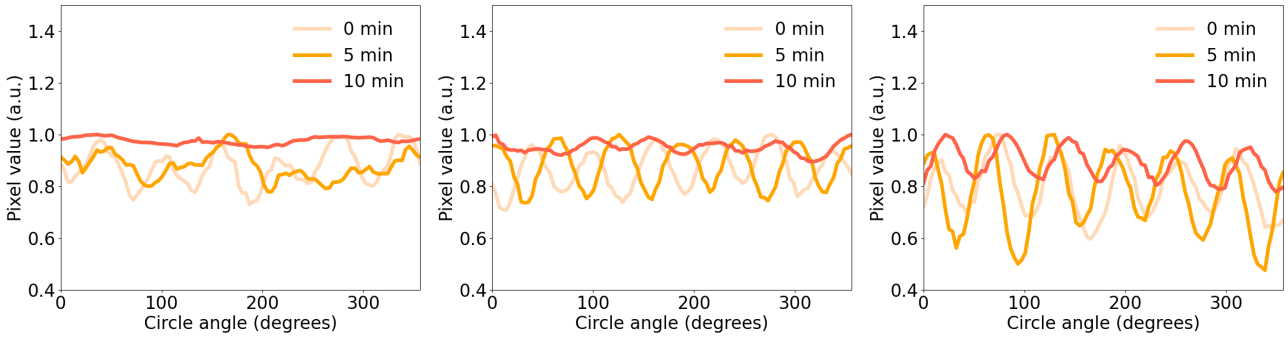

Figure 24: Normalized averaged circle height profile for 300 nm, 600 nm, and 800 nm nanospheres.

Furthermore, all profile data points are plotted in a boxplot in Figure 25a. The spread visualizes the earlier-mentioned difference in periodic height pattern amplitude. Additionally, the normalized averaged ratio of all samples with error bar is shown in Figure 25b. This graph shows the ratio trend after oxygen plasma exposure. A t-test has been performed on the normalized dataset to determine if there is a significant difference in profile after oxygen plasma exposure. The null hypothesis here is: there is no significant difference in profile after oxygen plasma exposure. Thus, the 0 min of oxygen plasma exposure was used as the control group with $\alpha = 0.05$. The results from the t-test are shown in Table 5. From the table, it can be concluded that the amplitude of the height pattern is highly significantly changed after 10 min of oxygen plasma exposure for all three nanosphere sizes. Furthermore, the difference after 5 min of oxygen plasma exposure for 300 nm nanosphere is just significant. However, there is no significant difference after 5 min of oxygen plasma exposure for 600 nm and 800 nm nanospheres. This data point is also an outlier in Figure 25b.

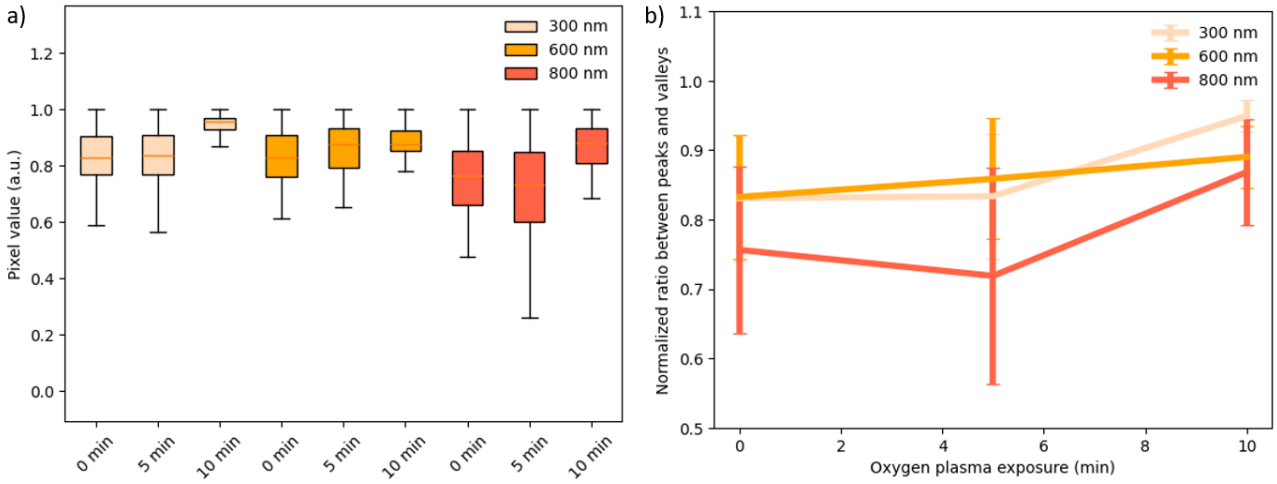

Figure 25: (a) Boxplot of gold layer morphology for 300 nm, 600 nm, and 800 nm nanospheres. (b) Normalized height valley ratio for different nanospheres after oxygen plasma exposure for different nanosphere sizes.

Table 5: T-test results on normalized data for the circle profiles, where each sample had 100 data points

Group	N	Mean	STD	t	p
Control 300 nm	5	60.9	4.83		
5 min 300 nm	5	143	8.39	-0.345	0.74
10 min 300 nm	5	61.3	0.84	-14.3	3.04e-21
Control 600 nm	5	84.8	7.36		
5 min 600 nm	5	116	10.3	-1.26	0.21
10 min 600 nm	5	145	3.62	-10.5	8.48e-21
Control 800 nm	5	73.8	9.44		
5 min 800 nm	5	135	25.1	1.43	0.15
10 min 800 nm	5	147	10.0	-8.13	4.70e-14

5.1.2 Gold islands via heat treatment

The alternative route to form nanoarrays is by melting the beads to reduce the gap between adjacent beads. Several experiments were performed to heat the glass to reach the T_g of 107 °C for the polystyrene nanospheres. For the first experiment, the glass substrate was heated on a hot plate with a small aluminum block for better heat transfer. A thermal probe was placed on top of the block's surface to measure its temperature. The glass substrate was heated for 20 seconds when the block had a stable temperature of 107 °C. An AFM image of the mask's surface is shown in Figure 26. It can be seen that the nanospheres lost their structural integrity due to the surface being warmer than 107°C.

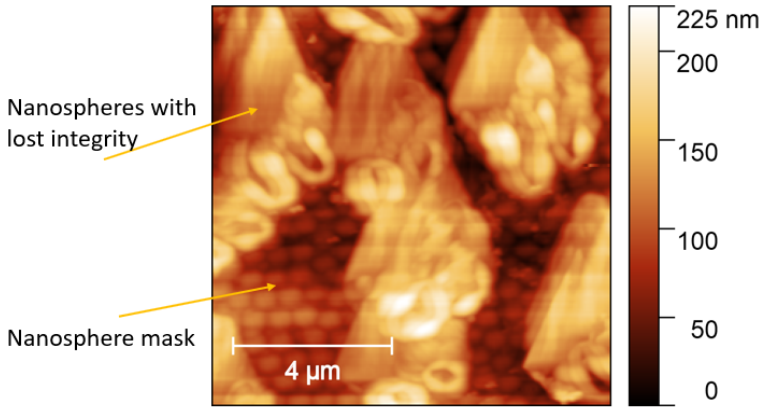

Figure 26: AFM image of nanosphere mask (600 nm) after heat treatment at 107°C for 20 seconds.

Since the thermal probe was not accurate in its reading, it was decided to rely on the knob settings of the hot plate. More measurements were performed around 100 °C with more prolonged heat exposure and around 150 °C with lower heat exposure. Here, the nanospheres were removed in toluene since the heating made the nanospheres fuse with the glass substrate and/or each other. An overview of AFM images for these experiments is shown in Figure 27

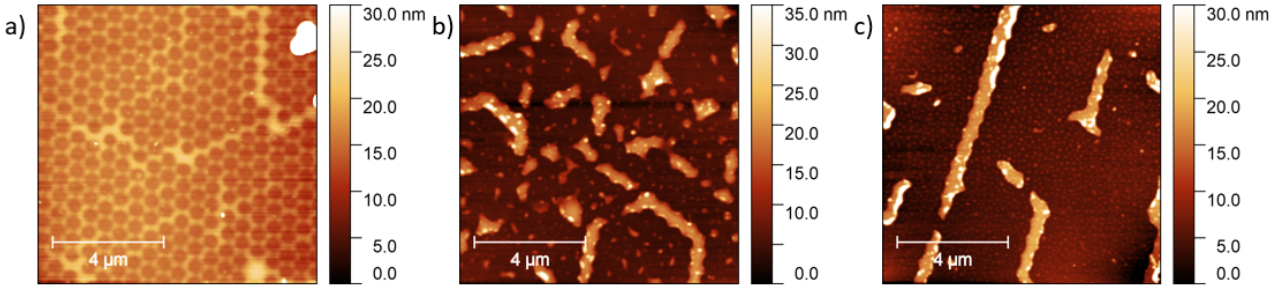

Figure 27: AFM image of surface after heat treatment (a) around 100 °C for 2 min (b) 150 °C for 3 s (c) 150 °C for 10 s. For all three images, 20 nm of gold was sputtered.

Visually, the results for 100 °C for 2 min look similar to those without heat treatment. The gold structures are still connected, but they are slightly thinner. This is also reflected in the average diameter of the non-exposed area, which is 411.6 nm compared to the average of 385.8 nm without heat treatment. As such, heating around 100 °C was not enough to create individual gold islands. Therefore, heating around 150 °C was performed to see the extremes of heating nanospheres well above their T_g. Here, the leftover structure had random small dot structures; however, these dot structures were not placed in a repetitive structure with equal spacing. Therefore, it is not the result of the mask but instead of the nanospheres collapsing at high temperatures.

A surface temperature sensor was used to improve the heat treatment's accuracy. This sensor was placed on the aluminum block while still leaving space for the glass substrates to be placed on the block. For these experiments, an SEM analysis was done on the hole size between nanospheres after heat treatment. This is done to find the heating effect on the nanospheres and how that affects the gold array. In Table 6, an overview of the hole diameter is given after heat treatment at 107 °C. The same Python code that was used for the

binding spot size was used here. The holes for the 25 s sample were so small that they could not be recognized by the code. The bigger outliers are shown in the table instead of the average for the 20 s sample.

Table 6: Overview of mean hole diameter for heating times at 107°C

Nanosphere/Melting	0 s	5 s	10 s	15 s	20 s	25 s	30 s	35 s	40 s
600 nm	175.3 nm	-	160.5 nm	111.1 nm	128.0 nm	103.4 nm	0 nm	0 nm	0 nm

Figure 28 shows an overview of SEM images illustrating the hole size between nanosphers of heat treatment at 107 °C. From the figure, it can be seen that the hole size decreases after heating the nanospheres. The relation between hole size and heating time is shown in Figure 28. It can be concluded that melting for 25 s reduces the hole size significantly while maintaining open holes. Compared to no heating, the hole size decreased by 33.5%. This was not the case for the samples that melted for 30 s or longer. Here, the holes are completely closed off.

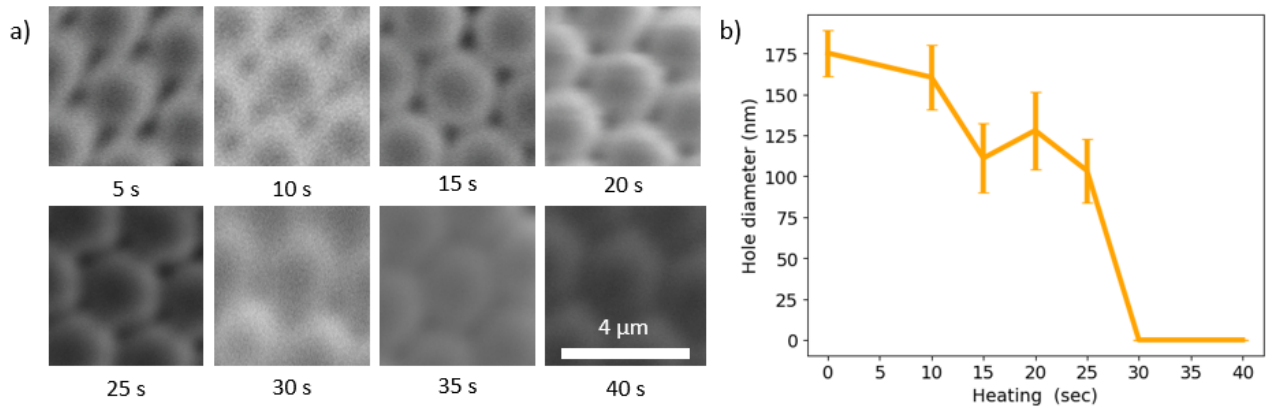

Figure 28: (a) AFM images of surface after heat treatment at 107 °C between 0 s and 40 s. (b) Graph showing the relationship between hole size and melting time.

However, these results are not entirely reliable. Due to uneven heating of the samples, some areas remained unaffected. The results partially considered these areas by using them as a size range. This is a user error; otherwise, this would have happened for multiple samples. It is possible that more pressure was applied to some areas when placing the sample on the aluminum block. Additionally, there was a discrepancy in all samples when measuring the heating time since it was performed manually. Some samples may have been heated longer or shorter than intended due to user errors while placing the sample, starting the timer, and removing the sample. This mainly caused the 20-second sample to have bigger holes than the 15-second sample.

After gold deposition and mask removal, individual gold islands appeared on the surface. Analysing the diameter was challenging, since the noise was of similar intensity. This is shown in Figure 29. The mean island size is significantly larger than the hole size. This is likely due to the random nature of magnetron gold sputter coating. Other deposition techniques, such as electron beam evaporation, would have the metal come perpendicularly to the mask and thus have a result similar to the hole size. However, this method of creating nanoarrays is also able to create 5x5 binding spot location consistently. Therefore, both methods can be used to achieve this research objective.

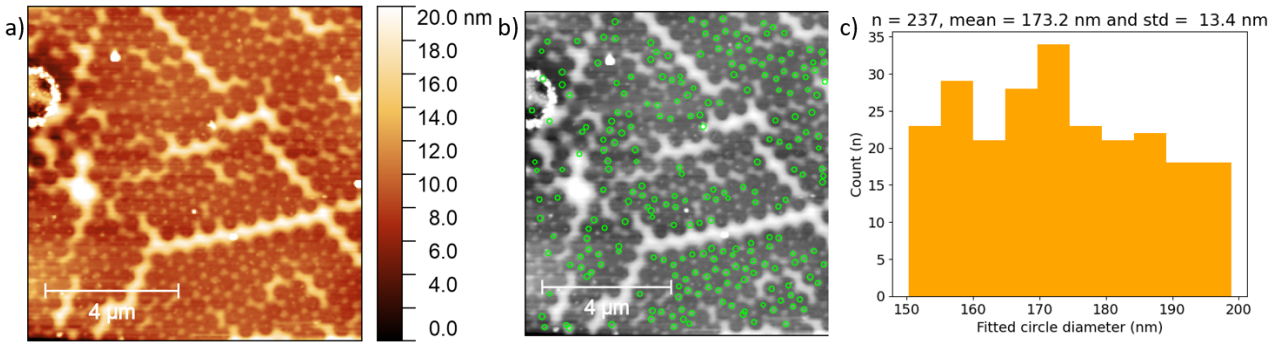

Figure 29: AFM image showing individual gold islands after heat treatment at 107 °C for 25 s, circles fitted on islands, and histogram showing spread in island size.

5.2 Fluorescence imaging of nanoarrays

Fluorescent measurements were performed on the arrays created in the previous section. Two types of DNA origami structures were used: a FRET ruler with an opening of 10 nucleotides (nt, equivalent to a ssDNA region of length 3.4 nm) and an HJ. A schematic overview of both structures is shown in Figure 6. Both structures had an ATTO647 and Cy3 FRET pair attached to the structure to monitor the presence and dynamic behaviour of the structure. This section uses two standard nanoarrays: 600 nm nanospheres with 10 min of oxygen plasma exposure for the reduced sphere size nanoarray with a 20 nm deposited gold layer. All fluorescent images in the subsection were taken with a 100 ms exposure time, without any gain, and with a laser operating at a 532 nm wavelength. The traces were then analyzed with iSMS [39].

5.2.1 Baseline: array without DNA origami

Before analysing any DNA origami structure in an array, baseline measurements were performed on: the reduced sphere size array with nanospheres still attached, the reduced sphere size array, and the reduced sphere size array with buffer. These measurements were performed to find the effect the array could have on experiments. The fluorescence baseline images for the reduced sphere size nanoarray are shown in Figure 30. It can be seen that all three images show autofluorescence; however, this effect is less intense in the image with the buffer. All three images were taken with the same laser intensity of 10 mW. Therefore, it can be seen in Figure 30c appears darker. This is due to the buffer absorbing the excited light.

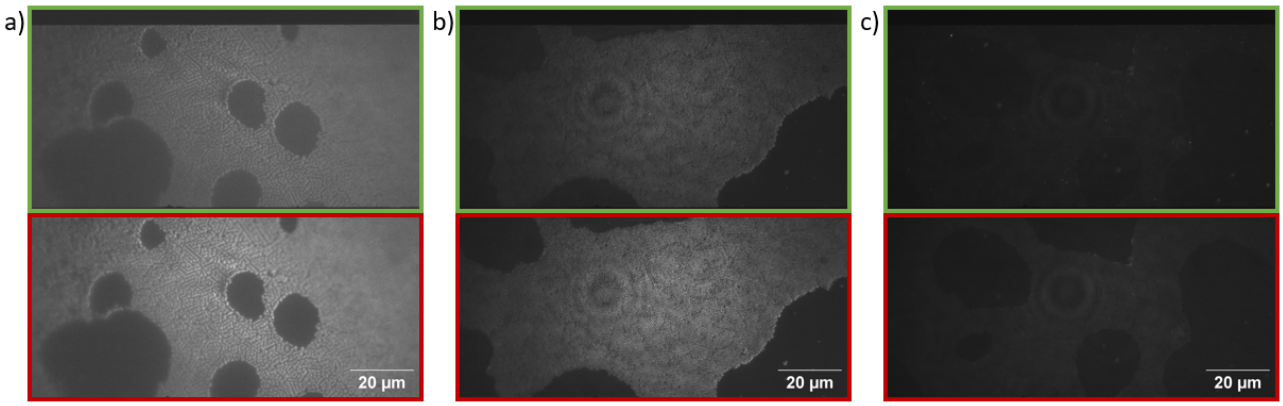

Figure 30: Baseline fluorescence images showing green (top) and red (bottom) channels at 10 mW laser power of (a) nanoarray with nanospheres, (b) nanoarray without nanospheres, (c) nanoarray with buffer. The three images have the same contrast setting.

More distinctive bright dots are shown in the image without nanospheres, representing the DNA origami's binding spots (glass surface). This surface looks very smooth compared to the sample with nanospheres still attached. Therefore, the remaining nanospheres on the surface can be identified by comparing them with the spheres shown in Figure 30a.

5.2.2 FRET rulers on glass

To have a reference of FRET traces for FRET rulers with 10 nt, baseline measurements were performed on glass without performing any modifications. Many measurements were performed with different batches of FRET rulers. However, when analyzing the data in more detail, some problems were found. The FRET pair of Cy3 and ATTO647 has a Förster radius of 4.56 nm [40]. Combined with Equation 1, this gives an expected FRET efficiency of 0.85. However, a value of 0.13 was found for all traces. Furthermore, the behavior of the donor and acceptor signal was directly correlated, while it should be anti-correlated. Therefore, all these measurements are deemed invalid. A fluorescent image with a corresponding FRET trace is shown in Figure 31. This problem is most likely caused by faulty ATTO647 fluorophores or using a completely different, incompatible fluorophore as an acceptor since there was a clear fluorescence signal from the acceptor, but not the donor. The signal found in the acceptor/red channel could be caused by the green fluorescence leaking into the red channel or an incorrect acceptor fluorophore.

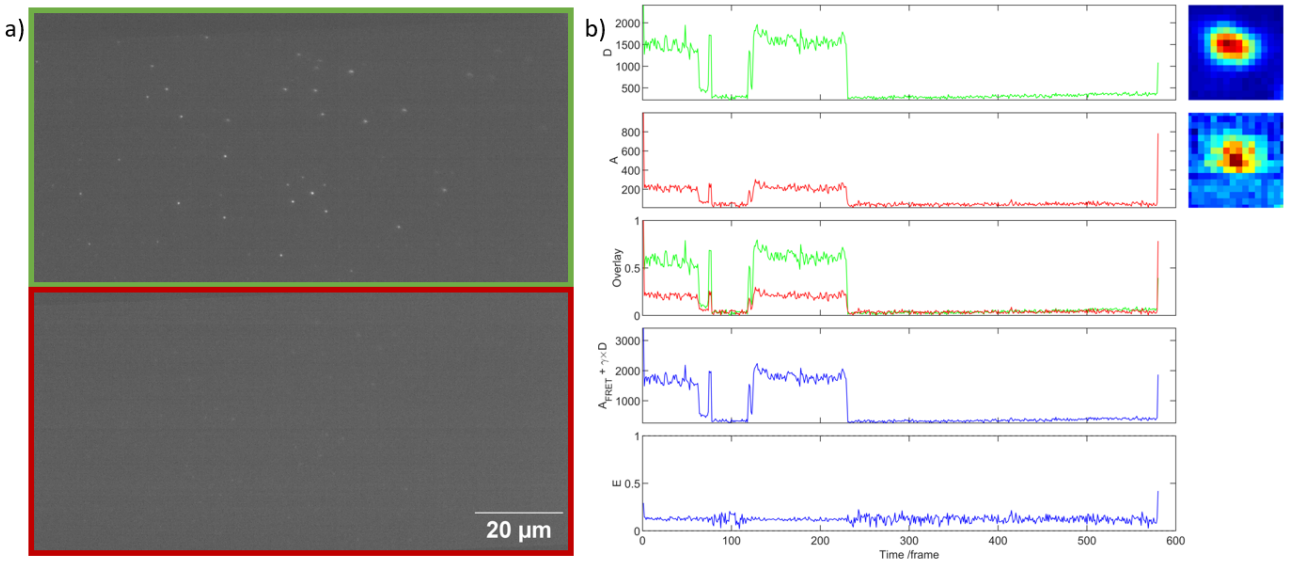

Figure 31: (a) Baseline fluorescence image of 10 nt FRET ruler at 4 mW laser power (b) Single trace showing with colocalized relation between donor and acceptor fluorophore.

Fortunately, it was possible to perform a single additional experiment with newly annealed FRET rulers. The FRET rulers used here had a gap of 2 nt; thus, a FRET efficiency of 0.99 is expected. This means almost no signal in the green channel and a strong signal in the red channel. The fluorescent image of these 2 nt FRET rulers with a corresponding FRET trace is shown in Figure 32. From the trace in Figure 32b, it can be seen that the average FRET efficiency is 0.96, as expected. However, many DNA origami structures are still visible in the green channel. Most of these spots did not have a corresponding acceptor signal. Therefore, these may be FRET rulers without an acceptor fluorophore.

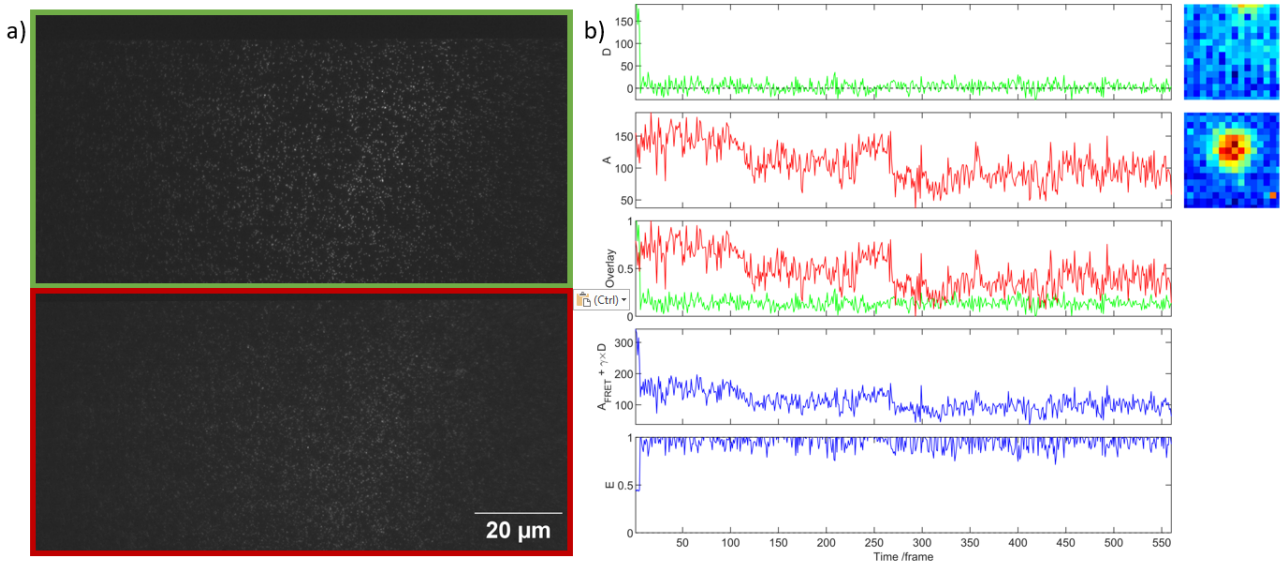

Figure 32: (a) Baseline fluorescence image of 2 nt FRET ruler at 2 mW laser power (b) Single trace showing with average FRET efficiency of 0.96.

For this experiment, only 150 pairs were analyzed since overlapping the green and red channels is hard for the software with a high FRET efficiency. There was a quality distribution in trace consistency compared to the trace shown in Figure 32b. About 12% of analyzed pairs give a similar signal, and another 8% had a high FRET efficiency while showing blinking behaviour. The other 80% did not have a consistently high FRET efficiency (bleaching was allowed), or their FRET efficiency was in the 0.10-0.80 range. Even though the FRET ruler structure is simple, the yield was low. This could be caused by the quality of the buffers used, which could also have a negative effect on the DNA origami structures, and whether the annealing procedure is good enough.

5.2.3 HJ on glass

The HJ suffered from the same problem as the early FRET ruler batches. The traces were correlated, there was no state switching, and the traces were similar to the '10 nt' FRET ruler trace. Fortunately, a single experiment was also able to show the expected state switching of an HJ. The results are shown in Figure 33. From Figure 33a, it can be seen that significantly fewer bright spots are visible compared to the FRET rulers while the samples were prepared with the same procedure simultaneously.

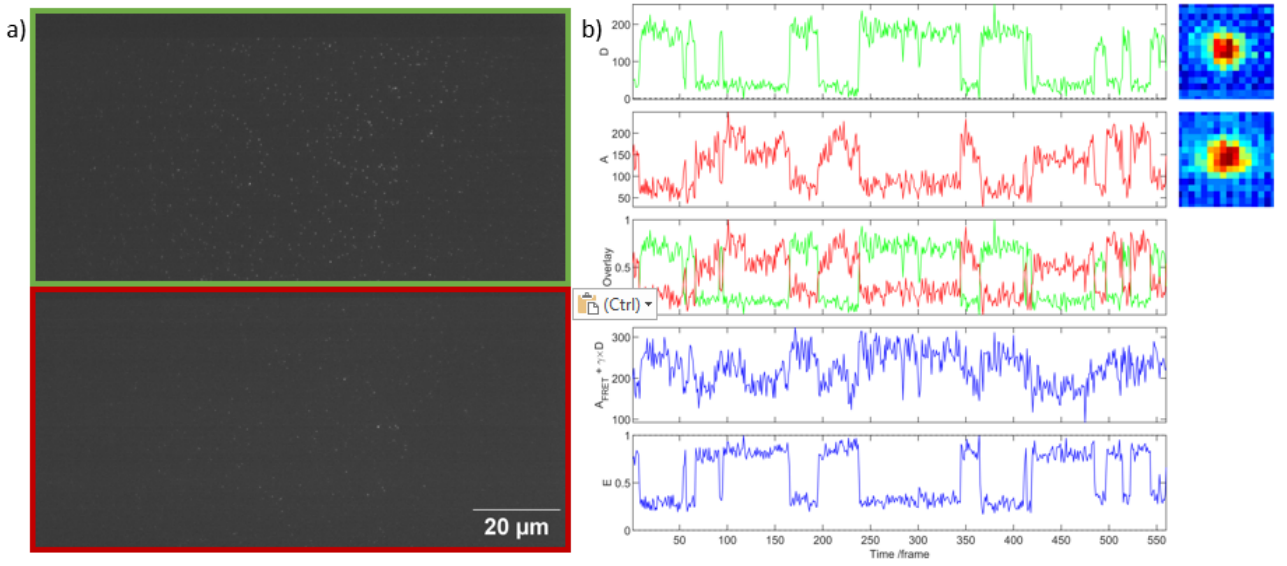

Figure 33: (a) Baseline fluorescence image of HJ at 2 mW laser power (b) Single trace showing switching states of HJ.

Also, here, the yield of the HJs was low. From the 200 pairs analyzed, only 5% showed distinctive state switching as shown in Figure 33b. The causes for low yield, like with the FRET rulers, are a bad quality of the buffer or an ineffective annealing procedure.

5.2.4 HJ in reduced sphere size array

The experiments with faulty DNA origami structures formed a strong foundation for the single experiment conducted with the reduced sphere size array. The early experiments were unsuccessful; no DNA origami structures were visible within the array. The images and videos of these experiments gave similar results as the baseline measurements of the array with only a buffer. This could have been caused by the extensive flushing during the preparation of the flowcell. This intensive flushing might have removed the biotin-BSA passivation layer. Therefore, it was chosen to reduce all the washing to 100 μL instead of 450 μL. Furthermore, the concentration of neutravidin was doubled to 1 mg/mL. This was done to ensure all the biotin-BSA molecules were functional for binding with the DNA origami structures. Finally, the DNA origami solution was diluted 2 times with buffer B to ensure better distribution of the DNA origami within the flowcell during incubation. This updated protocol was used for all three final experiments.

Two fluorescent images of HJs within the reduced sphere size array are shown in Figure 34. It can be seen that the fluorescence of the HJs is strong enough to create enough contrast with the autofluorescence from the array. Three distinctive intensities can be seen in Figure 34a. The dark region shows the boundaries of the gold array, the grey area is the gold array, and the bright spots are HJs or remaining nanospheres. In Figure 34b, many groups of remaining nanospheres are visible. These groups remained visible after increasing the laser power to 10 mW for 5 min. As such, it can be confirmed that these groups are nanospheres since they did not photobleach.

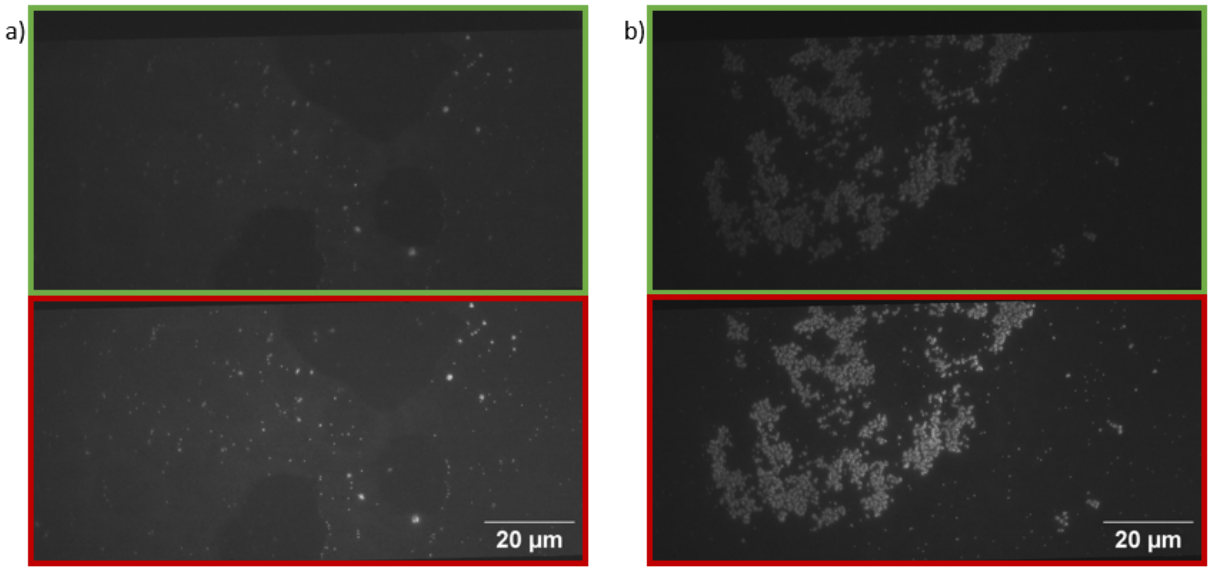

Figure 34: Fluorescent image of HJs within reduced sphere size array at 3.5 mW laser power (a) with little remaining nanospheres of 600 nm (b) with many remaining nanospheres of 600 nm. Here, the figures were individually adjusted for contrast.

Therefore, looking at the FRET traces is required to differentiate between HJs and nanospheres. From the 700 traces analyzed, only 5 HJs with switching states were found. The best trace is shown in Figure 35. The yield of immobilized HJ structures with switching states in the reduced sphere size array was ~0.7%. Based on the baseline results of HJ, there must be HJs present within the array that do not show switching states. There were ~4.3% of the traces with the same intensity of around 1000 a.u. on the sample. It can be said that the second research objective of achieving an occupancy of 50% within the array was not achieved. The low number of HJs within the array could be caused by leftover residue from the nanospheres on the glass, which prevents biotin-BSA from attaching to the glass surface. An additional step of oxygen plasma cleaning after sonication could remove this residue. Due to time constraints, it was not possible to try this new step. Additionally, when analyzing the remaining groups of nanospheres, they gave an intensity of around 500 a.u..

This is lower than the intensity of the HJ, and therefore, with the intensity, it is possible to distinguish between DNA origami structures and remaining nanospheres. The difference in intensity of HJ within the array (1000 a.u.) and baseline HJ (300 a.u.) is caused by the higher contrast in the images taken with the array.

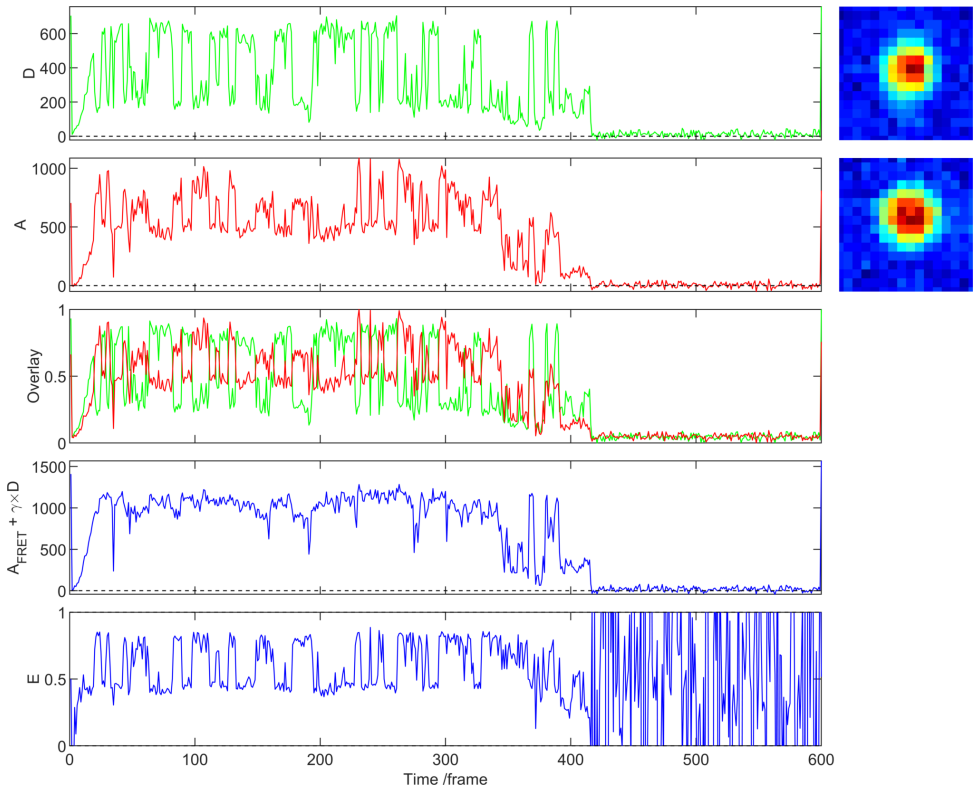

Figure 35: HJ trace when placed within reduced sphere size array.

Within the nanoarray, the analyzed traces were of high quality. The iSMS software could easily differentiate between the fluorescent signal and the background. The spacing between the binding spots was large enough. Additionally, no traces of increased intensity were caused by having multiple DNA origami structures within the exact location. If the immobilizing yield were higher, then analyzing the data would require minimal user input for selecting traces with potential crosstalk.

To achieve the third and last research objective of having the dynamics of the placed DNA origami structures not altered compared to randomly placed ones, a t-test is performed. Here, the null hypothesis is that there is no difference in FRET efficiency when an HJ is placed in an array compared to when it is not. $\alpha = 0.05$, and the control group consisted of 4 traces with each 400 data points. The part of the trace where the FRET efficiency was the highest over the 40 s was selected for both the control and the trace from the array. The results are shown in Table 7. Both traces in the array had t-value $\gg \alpha$ and thus the null hypothesis is not rejected. Meaning that the reduced sphere size nanoarray has no impact on the dynamics of the HJ.

Table 7: T-test results FRET traces

Group	N	Mean	STD	t	p
Control HJ	1600	0.58	0.26		
Trace array 1	400	0.59	0.19	0.59	0.56
Trace array 2	400	0.71	0.30	8.73	5.16e-18

6 Discussion and Recommendations

This section mentions some limitations found during the project. Besides limitations, recommendations will be given for future research within the topic of nanoarrays for DNA origami structures.

6.1 Discussion

6.1.1 Python code, size range effect and optimizer

The code used to analyze binding spot or hole size within the nanosphere mask of heat treatment plays an essential role in this thesis. The effect of user input for allowed circle size is significant, this was shown in section 5.1.1. During the thesis, the results from this code were subjected to many changes. When a small change was made in the contour detection method, for example, the earlier found results had to be updated. This also happened often when using the allowed size range variable. Constantly, it was required to manually find the correct setting for each image while constantly running a computationally demanding code. This time-consuming process and uncertainties in final results made working with the code not optimal.

Additionally, the code uses many loops to optimize the results for the maximum number of detected circles. This was only useful for images with very distinctive, sharp contours. Noisy photos, or pictures in dark conditions, did not benefit from this. Therefore, using different optimization criteria or incorporating a penalty function could have helped with the images that did not give satisfying results.

6.1.2 Low thresholds resulting in lower yield

The yield was low for immobilized FRET ruler on glass, HJ on glass, or HJ within a nanoarray. Finding nice traces over multiple videos was rare. Therefore, in iSMS, the threshold to find acceptors and donor signals was intentionally set very low. This was done to ensure the software would pick up all useful traces. However, the side effect of this approach is that many noisy background traces also show up. Due to time constraints, removing all these signals was impossible. Most of these signals were therefore not removed, and thus, a low yield became unavoidable. By slightly increasing the threshold, the yield would already become higher. Ideally, the threshold first has a low value to find all the desired traces and is then increased until a good trace gets removed. Unfortunately, this was not done due to time limits.

6.2 Recommendations

This research has demonstrated that gold nanoarrays can improve the quality of FRET traces for dynamic DNA origami structures. However, the use of nanoarrays for FRET measurements is still in its early stages, and therefore, I would recommend looking into the following research avenues for future research.

6.2.1 Non-toxic toluene alternative

The first research objective states that nanoarrays must be achieved using non-toxic chemicals. While gold sputtering already removes many other toxic substances, toluene is still used to sonicate nanospheres stuck on the surface. To make the use of nanoarrays more accessible to different labs, an alternative to toluene needs to be found. Alternatively, instead of a chemical process, a manufacturing process could also be used to create nanospheres attached to the glass surface.

6.2.2 Increase immobilization yield within array

The yield of HJ within the nanoarray was low. It is possible that biotin-BSA is not able to reach the binding spots due to interactions with the gold, both chemically and physically. It is also possible that the nanospheres leave a residue on the glass surface after removal. The presence of this residue, or the lack of biotin-BSA within the binding spots, needs to be further investigated.

6.2.3 Thiol bonding with gold island array

While a successful protocol was found for producing small gold dots (islands) with spacing in an array configuration, no fluorescent measurements were performed with these structures. Too much time was spent on performing experiments on the reduced sphere size array. To further improve the gold islands array, a more precise method for equally heating the nanospere mask needs to be found. Additionally, it is important to find

the correct incubation time ranges, since the self-assembly of thiol bonding with gold does not stop on its own. Then it is possible that too many DNA origami structures are present on a single gold island.

7 Conclusion

This thesis aimed to enhance the quality of FRET signals of DNA origami structures using a novel method involving gold nanoarrays and the immobilization of dynamic DNA origami structures within them. Firstly, nanoarrays with varying spacing were produced using the NSL technique. The quality of the nanosphere mask was partially optimized to improve the consistency and size of the gold nanoarrays. The reduced sphere size array, achieved with oxygen plasma exposure, and the gold island array, achieved with thermal treatment, were fabricated and analyzed. The effect of oxygen plasma exposure on different nanosphere sizes followed the same trend for increasing plasma exposure time; it resulted in a binding spot diameter as small as 191.1 nm for DNA origami structures while maintaining the same spacing. Partial melting of the nanospheres, at 107 °C for 25 s, reduced the hole size between them to a minimum of 60 nm. After sputtering, this resulted in regularly spaced small gold islands with a diameter of 173.2 nm. The custom Python code used to analyze both arrays gave consistent results. However, its performance was weak with low-contrast images. Therefore, based on quantitative and qualitative analysis, it can be concluded that the reduced sphere size and the gold island method are both valid for reliably producing nanoarrays with varying spacing and binding spot size. Furthermore, both methods were capable of producing an array with at least 5x5 binding spots. However, the removal of nanospheres was performed with sonication in toluene; neither method meets the requirement of using non-toxic chemicals. Still, the results are reproducible for other researchers without specialized equipment.

For the second part of this thesis, fluorescent measurements were performed with HJ on glass as a baseline and within the reduced sphere size array. Although HJs were placed within the array, they were found in ∼4.3% of 700 analyzed traces, while only ∼0.7% showed switching states. Therefore, the proposed method for immobilizing the DNA origami structures within the nanoarray has room for improvement. Strategies are discussed in the recommendation section. The second objective of achieving an occupancy of 50% within the nanoarray is not achieved. However, the third objective of not affecting the dynamics of DNA origami structures within a nanoarray was achieved. Two FRET efficiency traces had a t-value of 0.59 and 8.73, and therefore, the signal differences with the reference traces were not significant.

Finally, the main research question was: How can nanoarrays improve the data quality from FRET measurements of DNA origami structures? From this thesis, it can be said that nanoarrays improve the data quality from FRET measurements of DNA origami structures. The analyzed traces were differentiable with enough spacing to prevent crosstalk between samples. Also, no multiple DNA origami structures were found within the same binding spot. The dynamics of the immobilized DNA origami structures were not affected by placement within the reduced sphere size array. However, the proposed method cannot fill the nanoarray up to the desired 50% occupancy. While showing potential for its intended use, future research must look into increasing the yield when immobilizing DNA origami structures within the nanoarray.

References

[1] P. W. K. Rothemund, "Folding DNA to create nanoscale shapes and patterns," en, *Nature*, vol. 440, no. 7082, pp. 297–302, Mar. 2006, ISSN: 0028-0836, 1476-4687. DOI: 10.1038/nature04586. [Online]. Available: https://www.nature.com/articles/nature04586 (visited on 09/11/2024).

[2] M. Wanunu, "Nanopores: A journey towards DNA sequencing," en, *Physics of Life Reviews*, vol. 9, no. 2, pp. 125–158, Jun. 2012, ISSN: 15710645. DOI: 10.1016/j.plrev.2012.05.010. [Online]. Available: https://linkinghub.elsevier.com/retrieve/pii/S1571064512000395 (visited on 10/08/2024).

[3] J. Shim and L.-Q. Gu, "Single-molecule investigation of G-quadruplex using a nanopore sensor," eng, *Methods (San Diego, Calif.)*, vol. 57, no. 1, pp. 40–46, May 2012, ISSN: 1095-9130. DOI: 10.1016/j.ymeth.2012.03.026.

[4] N. An, A. M. Fleming, H. S. White, and C. J. Burrows, "Crown ether-electrolyte interactions permit nanopore detection of individual DNA abasic sites in single molecules," eng, *Proceedings of the National Academy of Sciences of the United States of America*, vol. 109, no. 29, pp. 11 504–11 509, Jul. 2012, ISSN: 1091-6490. DOI: 10.1073/pnas.1201669109.

[5] R. Duan, F. Xia, and L. Jiang, "Constructing Tunable Nanopores and Their Application in Drug Delivery," en, *ACS Nano*, vol. 7, no. 10, pp. 8344–8349, Oct. 2013, ISSN: 1936-0851, 1936-086X. DOI: 10.1021/nn405092w. [Online]. Available: https://pubs.acs.org/doi/10.1021/nn405092w (visited on 10/08/2024).

[6] D. Losic and S. Simovic, "Self-ordered nanopore and nanotube platforms for drug delivery applications," en, *Expert Opinion on Drug Delivery*, vol. 6, no. 12, pp. 1363–1381, Dec. 2009, ISSN: 1742-5247, 1744-7593. DOI: 10.1517/17425240903300857. [Online]. Available: https://www.tandfonline.com/doi/full/10.1517/17425240903300857 (visited on 10/08/2024).

[7] R. Roy, S. Hohng, and T. Ha, "A practical guide to single-molecule FRET," en, *Nature Methods*, vol. 5, no. 6, pp. 507–516, Jun. 2008, ISSN: 1548-7091, 1548-7105. DOI: 10.1038/nmeth.1208. [Online]. Available: https://www.nature.com/articles/nmeth.1208 (visited on 09/20/2024).

[8] D. K. Sasmal, L. E. Pulido, S. Kasal, and J. Huang, "Single-molecule fluorescence resonance energy transfer in molecular biology," en, *Nanoscale*, vol. 8, no. 48, pp. 19 928–19 944, 2016, ISSN: 2040-3364, 2040-3372. DOI: 10.1039/C6NR06794H. [Online]. Available: https://xlink.rsc.org/?DOI=C6NR06794H (visited on 09/20/2024).

[9] T. Kondo, W. J. Chen, and G. S. Schlau-Cohen, "Single-Molecule Fluorescence Spectroscopy of Photosynthetic Systems," en, *Chemical Reviews*, vol. 117, no. 2, pp. 860–898, Jan. 2017, ISSN: 0009-2665, 1520-6890. DOI: 10.1021/acs.chemrev.6b00195. [Online]. Available: https://pubs.acs.org/doi/10.1021/acs.chemrev.6b00195 (visited on 08/07/2025).

[10] Atushi, L, *Single Molecule Spectroscopy (SMS)*, Jun. 2010.

[11] A. Gopinath and P. W. K. Rothemund, "Optimized Assembly and Covalent Coupling of Single-Molecule DNA Origami Nanoarrays," en, *ACS Nano*, vol. 8, no. 12, pp. 12 030–12 040, Dec. 2014, ISSN: 1936-0851, 1936-086X. DOI: 10.1021/nn506014s. [Online]. Available: https://pubs.acs.org/doi/10.1021/nn506014s (visited on 03/05/2025).

[12] R. J. Kershner, L. D. Bozano, C. M. Micheel, *et al.*, "Placement and orientation of individual DNA shapes on lithographically patterned surfaces," en, *Nature Nanotechnology*, vol. 4, no. 9, pp. 557–561, Sep. 2009, ISSN: 1748-3387, 1748-3395. DOI: 10.1038/nnano.2009.220. [Online]. Available: https://www.nature.com/articles/nnano.2009.220 (visited on 03/05/2025).

[13] R. M. Shetty, S. R. Brady, P. W. K. Rothemund, R. F. Hariadi, and A. Gopinath, "Bench-Top Fabrication of Single-Molecule Nanoarrays by DNA Origami Placement," en, *ACS Nano*, vol. 15, no. 7, pp. 11 441–11 450, Jul. 2021, ISSN: 1936-0851, 1936-086X. DOI: 10.1021/acsnano.1c01150. [Online]. Available: https://pubs.acs.org/doi/10.1021/acsnano.1c01150 (visited on 12/09/2024).

[14] B. Saccà and C. M. Niemeyer, "DNA Origami: The Art of Folding DNA," en, *Angewandte Chemie International Edition*, vol. 51, no. 1, pp. 58–66, Jan. 2012, ISSN: 1433-7851, 1521-3773. DOI: 10.1002/anie.201105846. [Online]. Available: https://onlinelibrary.wiley.com/doi/10.1002/anie.201105846 (visited on 09/11/2024).

[15] H. Ijäs, S. Nummelin, B. Shen, M. A. Kostiainen, and V. Linko, "Dynamic DNA Origami Devices: From Strand-Displacement Reactions to External-Stimuli Responsive Systems," en, *International Journal of Molecular Sciences*, vol. 19, no. 7, p. 2114, Jul. 2018, ISSN: 1422-0067. DOI: 10.3390/ijms19072114. [Online]. Available: https://www.mdpi.com/1422-0067/19/7/2114 (visited on 09/11/2024).

[16] Z. Yu, A. V. Baptist, S. C. M. Reinhardt, *et al.*, "Compliant DNA Origami Nanoactuators as Size-Selective Nanopores," en, *Advanced Materials*, p. 2 405 104, Jul. 2024, ISSN: 0935-9648, 1521-4095. DOI: 10.1002/adma.202405104. [Online]. Available: https://onlinelibrary.wiley.com/doi/10.1002/adma.202405104 (visited on 09/11/2024).

[17] F. C. Simmel, B. Yurke, and H. R. Singh, "Principles and Applications of Nucleic Acid Strand Displacement Reactions," en, *Chemical Reviews*, vol. 119, no. 10, pp. 6326–6369, May 2019, ISSN: 0009-2665, 1520-6890. DOI: 10.1021/acs.chemrev.8b00580. [Online]. Available: https://pubs.acs.org/doi/10.1021/acs.chemrev.8b00580 (visited on 09/19/2024).

[18] A. Mooney, *Förster resonance energy transfer*, en, Page Version ID: 1273713346, Feb. 2025. [Online]. Available: https://en.wikipedia.org/w/index.php?title=F%C3%B6rster_resonance_energy_transfer&oldid=1273713346 (visited on 02/05/2025).

[19] C. Hyeon, J. Lee, J. Yoon, S. Hohng, and D. Thirumalai, "Hidden complexity in the isomerization dynamics of Holliday junctions," en, *Nature Chemistry*, vol. 4, no. 11, pp. 907–914, Nov. 2012, ISSN: 1755-4330, 1755-4349. DOI: 10.1038/nchem.1463. [Online]. Available: https://www.nature.com/articles/nchem.1463 (visited on 03/04/2025).

[20] Orekhova, D, *Holliday junction Trace*, 2024.

[21] A. L. Mattheyses, S. M. Simon, and J. Z. Rappoport, "Imaging with total internal reflection fluorescence microscopy for the cell biologist," en, *Journal of Cell Science*, vol. 123, no. 21, pp. 3621–3628, Nov. 2010, ISSN: 1477-9137, 0021-9533. DOI: 10.1242/jcs.056218. [Online]. Available: https://journals.biologists.com/jcs/article/123/21/3621/31390/Imaging-with-total-internal-reflection (visited on 03/04/2025).

[22] M. J. Rust, M. Bates, and X. Zhuang, "Sub-diffraction-limit imaging by stochastic optical reconstruction microscopy (STORM)," en, *Nature Methods*, vol. 3, no. 10, pp. 793–796, Oct. 2006, ISSN: 1548-7091, 1548-7105. DOI: 10.1038/nmeth929. [Online]. Available: https://www.nature.com/articles/nmeth929 (visited on 03/04/2025).

[23] A. Jimenez, K. Friedl, and C. Leterrier, *About samples, giving examples: Optimized Single Molecule Localization Microscopy*, en, Mar. 2019. DOI: 10.1101/568295. [Online]. Available: http://biorxiv.org/lookup/doi/10.1101/568295 (visited on 03/05/2025).

[24] J. Schnitzbauer, M. T. Strauss, T. Schlichthaerle, F. Schueder, and R. Jungmann, "Super-resolution microscopy with DNA-PAINT," en, *Nature Protocols*, vol. 12, no. 6, pp. 1198–1228, Jun. 2017, ISSN: 1754-2189, 1750-2799. DOI: 10.1038/nprot.2017.024. [Online]. Available: https://www.nature.com/articles/nprot.2017.024 (visited on 09/20/2024).

[25] P. R. Steen, E. M. Unterauer, L. A. Masullo, *et al.*, "The DNA-PAINT palette: A comprehensive performance analysis of fluorescent dyes," en, *Nature Methods*, vol. 21, no. 9, pp. 1755–1762, Sep. 2024, ISSN: 1548-7091, 1548-7105. DOI: 10.1038/s41592-024-02374-8. [Online]. Available: https://www.nature.com/articles/s41592-024-02374-8 (visited on 07/30/2025).

[26] C. L. Haynes and R. P. Van Duyne, "Nanosphere Lithography: A Versatile Nanofabrication Tool for Studies of Size-Dependent Nanoparticle Optics," en, *The Journal of Physical Chemistry B*, vol. 105, no. 24, pp. 5599–5611, Jun. 2001, ISSN: 1520-6106, 1520-5207. DOI: 10.1021/jp010657m. [Online]. Available: https://pubs.acs.org/doi/10.1021/jp010657m (visited on 01/14/2025).

[27] P. Colson, C. Henrist, and R. Cloots, "Nanosphere Lithography: A Powerful Method for the Controlled Manufacturing of Nanomaterials," en, *Journal of Nanomaterials*, vol. 2013, no. 1, T. Jiao, Ed., p. 948 510, Jan. 2013, ISSN: 1687-4110, 1687-4129. DOI: 10.1155/2013/948510. [Online]. Available: https://onlinelibrary.wiley.com/doi/10.1155/2013/948510 (visited on 02/11/2025).

[28] R. T. Aggarwal, L. Lai, and H. Li, "Microarray fabrication techniques for multiplexed bioassay applications," en, *Analytical Biochemistry*, vol. 683, p. 115 369, Dec. 2023, ISSN: 00032697. DOI: 10.1016/j.ab.2023.115369. [Online]. Available: https://linkinghub.elsevier.com/retrieve/pii/S0003269723003342 (visited on 01/14/2025).

[29] D. Qin, Y. Xia, and G. M. Whitesides, "Soft lithography for micro- and nanoscale patterning," en, *Nature Protocols*, vol. 5, no. 3, pp. 491–502, Mar. 2010, ISSN: 1754-2189, 1750-2799. DOI: 10.1038/nprot.2009.234. [Online]. Available: https://www.nature.com/articles/nprot.2009.234 (visited on 03/04/2025).

[30] D. B. Weibel, W. R. DiLuzio, and G. M. Whitesides, "Microfabrication meets microbiology," en, *Nature Reviews Microbiology*, vol. 5, no. 3, pp. 209–218, Mar. 2007, ISSN: 1740-1526, 1740-1534. DOI: 10.1038/nrmicro1616. [Online]. Available: https://www.nature.com/articles/nrmicro1616 (visited on 03/05/2025).

[31] C. Vieu, F. Carcenac, A. Pépin, *et al.*, "Electron beam lithography: Resolution limits and applications," en, *Applied Surface Science*, vol. 164, no. 1-4, pp. 111–117, Sep. 2000, ISSN: 01694332. DOI: 10.1016/S0169-4332(00)00352-4. [Online]. Available: https://linkinghub.elsevier.com/retrieve/pii/S0169433200003524 (visited on 03/04/2025).

[32] F. Watt, A. A. Bettiol, J. A. Van Kan, E. J. Teo, and M. B. H. Breese, "ION BEAM LITHOGRAPHY AND NANOFABRICATION: A REVIEW," en, *International Journal of Nanoscience*, vol. 04, no. 03, pp. 269–286, Jun. 2005, ISSN: 0219-581X, 1793-5350. DOI: 10.1142/S0219581X05003139. [Online]. Available: https://www.worldscientific.com/doi/abs/10.1142/S0219581X05003139 (visited on 03/04/2025).

[33] A. Gopinath, E. Miyazono, A. Faraon, and P. W. K. Rothemund, "Engineering and mapping nanocavity emission via precision placement of DNA origami," en, *Nature*, vol. 535, no. 7612, pp. 401–405, Jul. 2016, ISSN: 0028-0836, 1476-4687. DOI: 10.1038/nature18287. [Online]. Available: https://www.nature.com/articles/nature18287 (visited on 03/05/2025).

[34] A. Auer, M. T. Strauss, T. Schlichthaerle, and R. Jungmann, "Fast, Background-Free DNA-PAINT Imaging Using FRET-Based Probes," en, *Nano Letters*, vol. 17, no. 10, pp. 6428–6434, Oct. 2017, ISSN: 1530-6984, 1530-6992. DOI: 10.1021/acs.nanolett.7b03425. [Online]. Available: https://pubs.acs.org/doi/10.1021/acs.nanolett.7b03425 (visited on 02/11/2025).

[35] N. S. Deußner-Helfmann, A. Auer, M. T. Strauss, *et al.*, "Correlative Single-Molecule FRET and DNA-PAINT Imaging," en, *Nano Letters*, vol. 18, no. 7, pp. 4626–4630, Jul. 2018, ISSN: 1530-6984, 1530-6992. DOI: 10.1021/acs.nanolett.8b02185. [Online]. Available: https://pubs.acs.org/doi/10.1021/acs.nanolett.8b02185 (visited on 02/11/2025).

[36] P. Kelly and R. Arnell, "Magnetron sputtering: A review of recent developments and applications," en, *Vacuum*, vol. 56, no. 3, pp. 159–172, Mar. 2000, ISSN: 0042207X. DOI: 10.1016/S0042-207X(99)00189-X. [Online]. Available: https://linkinghub.elsevier.com/retrieve/pii/S0042207X9900189X (visited on 07/30/2025).

[37] N. A. Geisse, "AFM and combined optical techniques," en, *Materials Today*, vol. 12, no. 7-8, pp. 40–45, Jul. 2009, ISSN: 13697021. DOI: 10.1016/S1369-7021(09)70201-9. [Online]. Available: https://linkinghub.elsevier.com/retrieve/pii/S1369702109702019 (visited on 03/04/2025).

[38] W. Zhou, R. Apkarian, Z. L. Wang, and D. Joy, "Fundamentals of Scanning Electron Microscopy (SEM)," en, in *Scanning Microscopy for Nanotechnology*, W. Zhou and Z. L. Wang, Eds., New York, NY: Springer New York, 2006, pp. 1–40, ISBN: 978-0-387-33325-0 978-0-387-39620-0. DOI: 10.1007/978-0-387-39620-0_1. [Online]. Available: http://link.springer.com/10.1007/978-0-387-39620-0_1 (visited on 03/04/2025).

[39] S. Preus, S. L. Noer, L. L. Hildebrandt, D. Gudnason, and V. Birkedal, "iSMS: Single-molecule FRET microscopy software," en, *Nature Methods*, vol. 12, no. 7, pp. 593–594, Jul. 2015, ISSN: 1548-7091, 1548-7105. DOI: 10.1038/nmeth.3435. [Online]. Available: https://www.nature.com/articles/nmeth.3435 (visited on 08/14/2025).

[40] T. J. Lambert, "FPbase: A community-editable fluorescent protein database," en, *Nature Methods*, vol. 16, no. 4, pp. 277–278, Apr. 2019, ISSN: 1548-7091, 1548-7105. DOI: 10.1038/s41592-019-0352-8. [Online]. Available: https://www.nature.com/articles/s41592-019-0352-8 (visited on 08/13/2025).